Improved ski pole design by thin-ply composite reinforcement

Master's thesis in Applied Mechanics

MARTIN GRANLUND
GUSTAV GRÄSBERG

Department of Applied mechanics
CHALMERS UNIVERSITY OF TECHNOLOGY
Göteborg, Sweden 2017

MASTER'S THESIS IN APPLIED MECHANICS

Improved ski pole design by thin-ply composite reinforcement

MARTIN GRANLUND
GUSTAV GRÄSBERG

Department of Applied mechanics
Division of Material and Computational Mechanics
CHALMERS UNIVERSITY OF TECHNOLOGY

Göteborg, Sweden 2017

Improved ski pole design by thin-ply composite reinforcement
MARTIN GRANLUND
GUSTAV GRÄSBERG

Master's thesis 2017:29
ISSN 1652-8557
Department of Applied mechanics
Division of Material and Computational Mechanics
Chalmers University of Technology
SE-412 96 Göteborg
Sweden
Telephone: +46 (0)31-772 1000

Cover:
Skigo Race 2.0 cross-country ski pole

Chalmers Reproservice
Göteborg, Sweden 2017

Improved ski pole design by thin-ply composite reinforcement
Master's thesis in Applied Mechanics
MARTIN GRANLUND
GUSTAV GRÄSBERG
Department of Applied mechanics
Division of Material and Computational Mechanics
Chalmers University of Technology

Abstract

For cross-country skiers, the ski poles are an essential tool for propulsion. To minimize the energy required for handling, the ski poles are to be light and stiff. The pursuit of lighter and stiffer ski poles has introduced Carbon Fiber Reinforced Plastics (CFRP) as the material class of choice. It has superior weight to stiffness properties compared to aluminum which is used for more basic ski poles. However, CFRP ski poles suffer from increased brittleness, whereby even small impacts may lead to sudden ski pole failure when it is used.

By experimentally analyzing two generations of Skigo race 2.0 ski poles, the mechanical behavior in terms of stiffness and impact resistance has been characterized. The behavior from the experiments was captured using Finite Element (FE) simulations. The simulations were then used as a tool for generating new concept ski poles. Experiments were also conducted on the reference ski poles to obtain material properties used in the FE models.

The project resulted in two concepts for more impact resistant ski poles which both have maintained weight and stiffness properties compared to the reference ski poles. To achieve this, the concept ski poles utilizes thin-ply CFRP and are arranged with and without a foam core. The intention of the concepts is to prove the benefits of using thin-ply CFRP to achieve increased impact resistance.

Proceeding from the concept, prototypes need to be manufactured and tested to verify performance and before a potential commercialization the concepts suitability for mass manufacturing has to be evaluated.

Keywords: ski pole, carbon fiber, CFRP, impact resistance, thin-ply, finite elements

Preface

This master's thesis was done at the department of Applied Mechanics at Chalmers University of Technology. It was written in collaboration with Skigo, who supplied ski poles for testing, and Oxeon who assisted with material and modeling knowledge for thin-ply CFRP.

We want to give a special thanks to examiner Martin Fagerström and supervisor Hana Zrida, you have been very supportive and your teachings have been invaluable. We would also like to thank Johan Ahlström, Knut Andreas Meyer, Dennis Wilhelmsson, Elanghovan Natesan, Andreas Karlsson and Stefan Norling for assisting in the project.

Gustav Gräsberg and Martin Granlund
Gothenburg, June 2017

Nomenclature

CFRP - Carbon Fiber Reinforced Plastic
FE - Finite Element
CAD - Computer Aided Design
ACP - Ansys Composite PrepPost
Prepreg - Pre-impregnated composite
CDM - Continuum Damage Mechanic
E_{L} - Longitudinal stiffness modulus
E_{T} - Transverse stiffness modulus
$E_{\mathrm{T'}}$ - Through-thickness stiffness modulus
G_{LT} - In-plane shear modulus
$G_{\mathrm{LT'}}$ - Transverse shear modulus
$G_{\mathrm{TT'}}$ - Through-thickness shear modulus
σ_{LU} - Longitudinal ultimate tensile strength
σ'_{LU} - Longitudinal ultimate compressive strength
σ_{TU} - Transverse ultimate tensile strength
σ'_{TU} - Transverse ultimate compressive strength
$\sigma_{T'U}$ - Through-thickness ultimate tensile strength
$\sigma'_{T'U}$ - Through-thickness ultimate compressive strength
$\varepsilon'_{\mathrm{LU}}$ - Longitudinal ultimate compressive strain
τ_{LTU} - In-plane ultimate shear strength
$\tau_{\mathrm{LT'U}}$ - Transverse ultimate shear strength
$\tau_{\mathrm{TT'U}}$ - Through-thickness ultimate shear strength
A_{f} - Fiber area fraction
a_{f} - Fiber area
A_{m} - Matrix area fraction
a_{m} - Matrix area
A_{v} - Void area fraction
a_{v} - Void area
a_{c} - Composite area

Contents

Figures

1 Introduction

Cross-country skiing has a long tradition in Scandinavia. Historically, mainly being a way to transverse the snow it has today developed into a major Olympic sport. Naturally, the equipment has followed the development and today materials such as Carbon Fiber Reinforced Plastics (CFRP) are often used. The design process of the equipment, however, are in many cases heuristic and based on experience rather than simulations. This thesis aims to take a more theoretical approach to further aid in the development of cross-country ski poles from an engineering point of view.

1.1 Background

To maximize the potential of athletes, the equipment has to be optimized. For cross-country skiers, the ski poles are an essential tool for propulsion. These are to be light and stiff to minimize the energy required for handling. Modern high end ski poles are manufactured from CFRP, they have higher stiffness and strength to weight ratio compared to more basic aluminum ski poles. However, CFRP ski poles suffer from increased brittleness. Such brittleness can have devastating consequences with ski poles being more susceptible to failure following an impact. Thus, there is a strong need to find the optimal design for CFRP ski poles with a good balance between weight, inertia, stiffness and impact resistance.

During the spring of 2016, a bachelor´s thesis [1] was written at Chalmers cooperating with Dala Sports Academy and the Swedish skiing equipment provider Skigo. The project resulted in a conceptual ski pole design with more optimized performance than the reference ski pole, the latter can be seen Figure 1.1. Suggestions for improvements were based on basic finite elements simulations. Test specimens were manufactured and tested. It could be concluded that performance improvements could be achieved simply by varying the CFRP lay-up sequence [1].

Figure 1.1: *Skigo Race 2.0 reference ski pole*

1.2 Purpose

Taking in to consideration the results from the bachelor's thesis [1], this thesis aims to further improve the impact resistance of ski poles by optimizing the composite lay-up and by utilizing thin-ply composites. New concepts for ski poles will be evaluated using numerical simulations supported by experiments.

1.3 Limitations

This thesis aims only to deliver a concept design considering CFRP materials and geometry alternations for the pole. Thus, the handle and basket of the pole has not been considered for improvement.

1.4 Goal

The proposed concept is targeted to be more impact resistant than the reference ski poles, whilst maintaining performance in terms of weight and stiffness.

2 Theory

In subsequent sections the relevant theory for the thesis is presented. The appellation of the different components of the ski poles are illustrated in Figure 2.1. The global coordinate system was defined such that the Z-axis is lengthwise of the pole with origin at the center of pole boundary on the basket end.

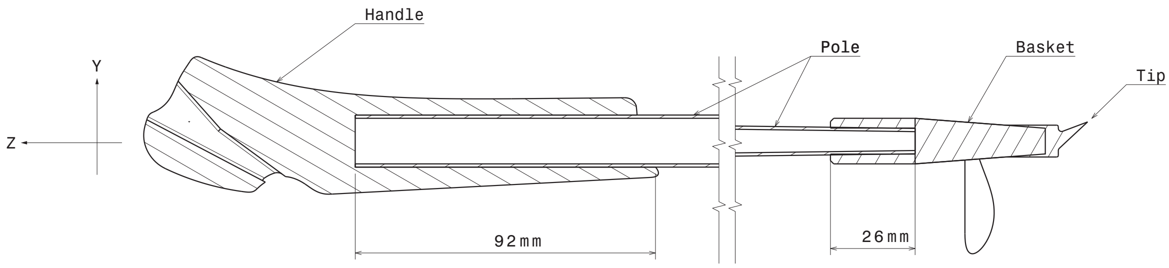

Figure 2.1: *X-Z cross cut of reference ski pole with measured values in global coordinates*

In Figure 2.2, a sketch of a ski pole cross-section is shown with its nomenclature.

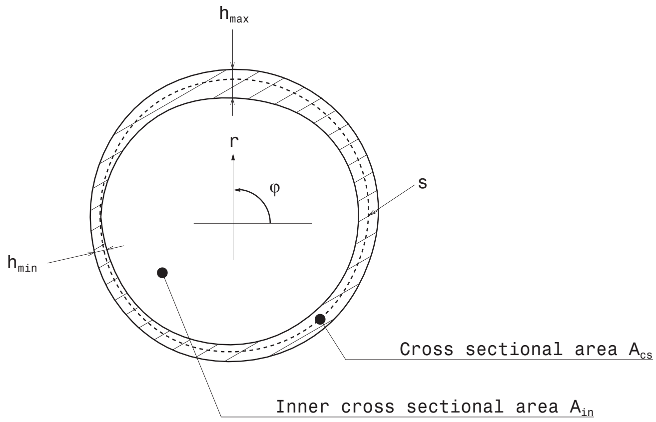

Figure 2.2: *r-φ cross-section of pole in local coordinates*

For the pole, a local coordinate system with polar coordinates is used, see Figure 2.2. This coordinate system is defined with origin in the center of the pole, with the Z-axis parallel to the global Z-axis.

2.1 Composite laminates

A composite laminate is a material created by layering multiple fiber reinforced sheets. These sheets are called *laminas* and by configuring these in different orientations, *laminates* with desired properties are obtained. In this thesis, the orientation of a lamina is defined by its angle relative to the Z-axis, as can be seen in Figure 2.3. This means that a lamina oriented at 0° has its fibers lengthwise of the ski pole. The orientation sequence of laminas is called a laminates lay-up. As an example, in Figure 2.3 the lay-up is [0/45/90].

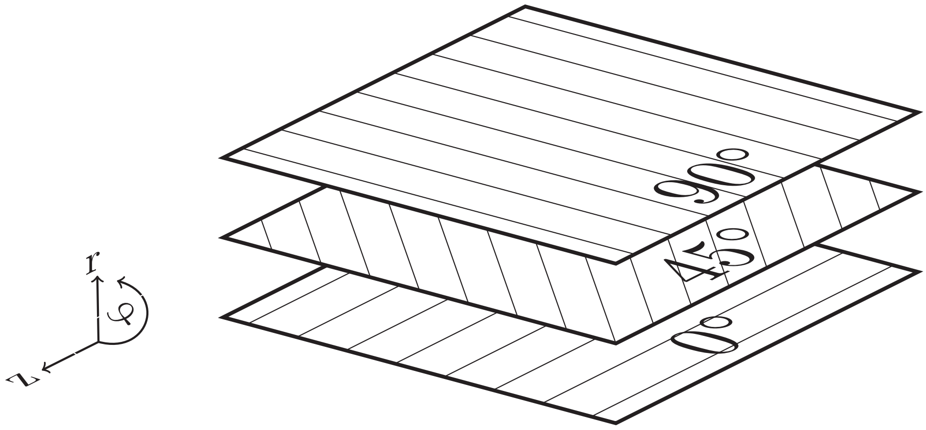

Figure 2.3: *Laminate with lamina lay-up sequence* [0/45/90]

Laminates are counted in positive radial direction in the local polar coordinate system. Meaning that the first lamina is closest to the center of the ski pole.

For a unidirectional ply where the fibers are aligned with the Z-axis, the transverse direction is defined as the circumferential direction φ and the through-thickness direction is in the radial direction r in the local coordinate system.

2.1.1 Composite lay-ups

A composite has anisotropic material properties, i.e. the elastic properties of the material have directional dependence, opposed to materials with isotropic material properties. A subset to anisotropic materials are transversely isotropic materials, which is the state for the composites in this thesis. The nomenclature for the material properties is as follows: The properties in the direction of the fibers have subscript L while subscript T represents the transverse direction. The through thickness properties are denoted with T′. Some material properties, such as the ultimate strength $\sigma_{\alpha\mathrm{U}}$ (where α = L,T,T′) not only have directional dependence but also have dependence on compression and tension loading. The annotation for compressive properties includes an apostrophe in the term, e.g. $\sigma'_{T'U}$ for the through-thickness ultimate compressive strength.

2.1.2 Orthotropic material

Orthotropic materials have three planes of symmetry. Elastic properties normal to such a plane do not change when the direction is reversed. An example is a fibre reinforced composite where r and φ are the in-plane axes and Z the axis normal to the plane. The lamina then exhibit the same elastic properties in the $\pm r$ direction with the plane of symmetry being the $\varphi - Z$ plane. In the same way elastic properties in the $\pm\varphi$ and in the $\pm Z$ direction are the same with the plane of symmetry being the $r - Z$ and the $r - \varphi$ plane, respectively.

When modeling an orthotropic material, nine independent material constants are required [2]

$$\begin{bmatrix} \sigma_\mathrm{z} \\ \sigma_\varphi \\ \sigma_\mathrm{r} \\ \tau_{\varphi\mathrm{r}} \\ \tau_\mathrm{zr} \\ \tau_{\mathrm{z}\varphi} \end{bmatrix} = \begin{bmatrix} C_{11} & C_{12} & C_{13} & 0 & 0 & 0 \\ C_{12} & C_{22} & C_{23} & 0 & 0 & 0 \\ C_{13} & C_{23} & C_{33} & 0 & 0 & 0 \\ 0 & 0 & 0 & C_{44} & 0 & 0 \\ 0 & 0 & 0 & 0 & C_{55} & 0 \\ 0 & 0 & 0 & 0 & 0 & C_{66} \end{bmatrix} \begin{bmatrix} \varepsilon_\mathrm{z} \\ \varepsilon_\varphi \\ \varepsilon_\mathrm{r} \\ \gamma_{\varphi\mathrm{r}} \\ \gamma_\mathrm{zr} \\ \gamma_{\mathrm{z}\varphi} \end{bmatrix} . \tag{2.1}$$

A special case of an orthotropic material is a transversely isotropic material which have one plane of isotropy. An example is the unidirectional fibre reinforced composite. In this case, all elastic properties which are orthogonal to the fibre direction are considered the same. Thus, the elastic properties in the transverse direction are the same as in the through-thickness direction. As a consequence modeling an elastic transversely isotropic material requires five independent material constants [2]

$$\begin{bmatrix}\sigma_{\mathrm{z}}\\ \sigma_{\varphi}\\ \sigma_{\mathrm{r}}\\ \tau_{\varphi\mathrm{r}}\\ \tau_{\mathrm{zr}}\\ \tau_{\mathrm{z}\varphi}\end{bmatrix} = \begin{bmatrix} C_{11} & C_{12} & C_{12} & 0 & 0 & 0\\ C_{12} & C_{22} & C_{23} & 0 & 0 & 0\\ C_{12} & C_{23} & C_{22} & 0 & 0 & 0\\ 0 & 0 & 0 & \frac{C_{22}-C_{23}}{2} & 0 & 0\\ 0 & 0 & 0 & 0 & C_{66} & 0\\ 0 & 0 & 0 & 0 & 0 & C_{66}\end{bmatrix} \begin{bmatrix}\varepsilon_{\mathrm{z}}\\ \varepsilon_{\varphi}\\ \varepsilon_{\mathrm{r}}\\ \gamma_{\varphi\mathrm{r}}\\ \gamma_{\mathrm{zr}}\\ \gamma_{\mathrm{z}\varphi}\end{bmatrix}. \tag{2.2}$$

2.1.3 Constitutive relation

In order to relate a global stress or strain to the local fiber oriented coordinate system the following transformations must be performed

$$\begin{bmatrix}\sigma_{\mathrm{L}}\\ \sigma_{\mathrm{T}}\\ \tau_{\mathrm{LT}}\end{bmatrix} = \boldsymbol{T}_1 \begin{bmatrix}\sigma_{\mathrm{z}}\\ \sigma_{\varphi}\\ \tau_{\mathrm{z}\varphi}\end{bmatrix} \tag{2.3}$$

$$\begin{bmatrix}\varepsilon_{\mathrm{L}}\\ \varepsilon_{\mathrm{T}}\\ \gamma_{\mathrm{LT}}\end{bmatrix} = \boldsymbol{T}_2 \begin{bmatrix}\varepsilon_{\mathrm{z}}\\ \varepsilon_{\varphi}\\ \gamma_{\mathrm{z}\varphi}\end{bmatrix} \tag{2.4}$$

where $\boldsymbol{T}_1$ and $\boldsymbol{T}_2$ are the stress and strain transformation matrices [2]. The relation between stresses and strains in the global coordinates thus becomes

$$\begin{bmatrix}\sigma_{\mathrm{z}}\\ \sigma_{\varphi}\\ \tau_{\mathrm{z}\varphi}\end{bmatrix} = \underbrace{\boldsymbol{T}_1^{-1}\boldsymbol{Q}\boldsymbol{T}_2}_{=\overline{\boldsymbol{Q}}} \begin{bmatrix}\varepsilon_{\mathrm{z}}\\ \varepsilon_{\varphi}\\ \gamma_{\mathrm{z}\varphi}\end{bmatrix}. \tag{2.5}$$

where $\boldsymbol{Q}$ is the ply stiffness matrix [2] and $\overline{\boldsymbol{Q}}$ is the ply stiffness transformed to the global coordinate system.

2.2 Failure in composites

There exist several criteria to predict failure in composites subjected to multi-axial loading. Within this thesis, the Hashin failure criterion has been used since it doesn't requires any additional material parameters than the ultimate stresses and takes load interaction into account. The Hashin failure criterion consists of five expressions to predict different failure modes [3]. The failure modes are:

Fiber direction tensile failure

$$\left(\frac{\sigma_{\mathrm{L}}}{\sigma_{\mathrm{LU}}}\right)^2 + \left(\frac{\tau_{\mathrm{LT}}}{\tau_{\mathrm{LTU}}}\right)^2 + \left(\frac{\tau_{\mathrm{LT'}}}{\tau_{\mathrm{LT'U}}}\right)^2 \geq 1. \tag{2.6}$$

Fiber direction compressive failure

$$-\frac{\sigma_{\mathrm{L}}}{\sigma'_{\mathrm{LU}}} \geq 1. \tag{2.7}$$

Transverse direction matrix tensile failure

$$\left(\frac{\sigma_{\mathrm{T}}}{\sigma_{\mathrm{TU}}}\right)^2 + \left(\frac{\tau_{\mathrm{LT}}}{\tau_{\mathrm{LTU}}}\right)^2 + \left(\frac{\tau_{\mathrm{LT'}}}{\tau_{\mathrm{LT'U}}}\right)^2 + \left(\frac{\tau_{\mathrm{TT'}}}{\tau_{\mathrm{TT'U}}}\right)^2 \geq 1. \tag{2.8}$$

Transverse direction matrix compressive failure

$$\left(\frac{\sigma_{\mathrm{T}}}{2\tau_{\mathrm{TT'U}}}\right)^2 + \left(\frac{\tau_{\mathrm{TT'}}}{\tau_{\mathrm{TT'U}}}\right)^2 + \left(\frac{\tau_{\mathrm{LT}}}{\tau_{\mathrm{LTU}}}\right)^2 + \left[\left(\frac{\sigma_{\mathrm{TU}}}{2\tau_{\mathrm{TT'U}}}\right)^2 - 1\right]\frac{\sigma_{\mathrm{T}}}{\sigma_{\mathrm{TU}}} \geq 1. \tag{2.9}$$

Delamination

$$\left(\frac{\sigma_{\mathrm{T'}}}{\sigma_{\mathrm{T'U}}}\right)^2 + \left(\frac{\tau_{\mathrm{LT'}}}{\tau_{\mathrm{LT'U}}}\right)^2 + \left(\frac{\tau_{\mathrm{TT'}}}{\tau_{\mathrm{TT'U}}}\right)^2 \geq 1, \quad \sigma_{\mathrm{T'}} > 0. \tag{2.10}$$

In the case of a sandwich structure an additional failure criteria for the core [4] is used and formulated as

$$\frac{|\tau_{\mathrm{LT'}}|}{\tau_{\mathrm{LT'U}}} + \frac{|\tau_{\mathrm{TT'}}|}{\tau_{\mathrm{TT'U}}} \geq 1, \quad \sigma_{\mathrm{T'}} \leq 0 \tag{2.11}$$

$$\frac{|\tau_{\mathrm{LT'}}|}{\tau_{\mathrm{LT'U}}} + \frac{|\tau_{\mathrm{TT'}}|}{\tau_{\mathrm{TT'U}}} + \frac{\sigma_{\mathrm{T'}}}{\sigma_{\mathrm{T'U}}} \geq 1, \quad \sigma_{\mathrm{T'}} > 0. \tag{2.12}$$

2.3 Damage modeling

Progressive damage in composites is a complex mechanism due to the orthotropic nature of the material. For this thesis, a simple damage model called Material Property Degradation (MPDG) has been used [5]. This model instantly reduces the stiffness of an element when a failure criterion has been met. The damaged stiffness matrix is formulated as

$$\boldsymbol{C}_{\mathrm{d}} = \begin{bmatrix} \frac{S_{11}}{1-d_f} & S_{12} & S_{13} & 0 & 0 & 0 \\ S_{12} & \frac{S_{22}}{1-d_m} & S_{23} & 0 & 0 & 0 \\ S_{13} & S_{23} & \frac{S_{33}}{1-d_m} & 0 & 0 & 0 \\ 0 & 0 & 0 & \frac{S_{44}}{1-d_s} & 0 & 0 \\ 0 & 0 & 0 & 0 & \frac{S_{55}}{1-d_s} & 0 \\ 0 & 0 & 0 & 0 & 0 & \frac{S_{66}}{1-d_s} \end{bmatrix}^{-1} \tag{2.13}$$

where d_f, d_m and d_s are the fiber, matrix and shear damage variables and $\boldsymbol{S}$ is the compliance matrix. The damage variables can vary between 0 and 1 where 1 indicates complete loss of stiffness. The value of the fiber and matrix damage variables are predefined by the user as

$$d_f = \begin{cases} d_f^+ & \text{for tension} \\ d_f^- & \text{for compression} \end{cases} \tag{2.14}$$

$$d_m = \begin{cases} d_m^+ & \text{for tension} \\ d_m^- & \text{for compression.} \end{cases} \tag{2.15}$$

Thus, the model requires four input parameters, one for each mode described above. The shear damage variable is calculated as

$$d_s = 1 - (1 - d_f^+)(1 - d_f^-)(1 - d_m^+)(1 - d_m^-). \tag{2.16}$$

2.4 Ski pole stiffness

In this thesis, the stiffness of a ski pole refers to the pole's resistance to bending. To understand the properties that affects the stiffness of a ski pole, it can be simplified to a simply supported beam with isotropic properties, see Figure 2.4.

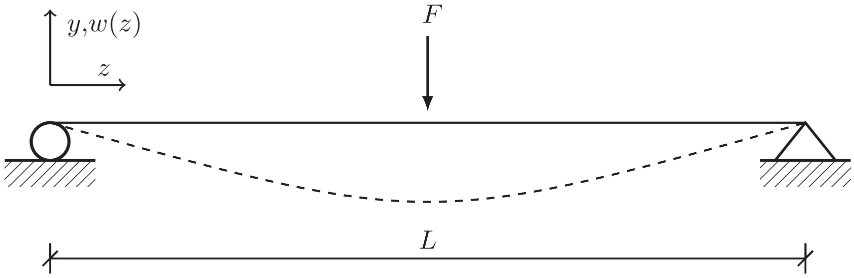

Figure 2.4: *Loaded simply supported beam*

Assuming small deformations, Euler-Bernoulli beam theory gives the maximum deflection $w_{\max} = w(L/2)$ as [6]

$$w_{\max} = \frac{FL^3}{48EI}. \tag{2.17}$$

It is observed that for a set length L and load F, increasing either the material stiffness E or the cross-sectional area moment of inertia I will decrease the deflection w_{max}, thus, the stiffness increases. The subsequent sections will discuss each of the properties.

2.4.1 Material stiffness

The material stiffness is defined as the material's ability to resist deformation. The stiffness can be divided into two major types; stiffness modulus E and shear stiffness modulus G. For an orthotropic material there are three planes of symmetry and thus a stiffness modulus and shear modulus corresponding to each plane, as discussed in Chapter 2.1.2.

Stiffness modulus E

For a member with the cross-sectional area A_{CS} axially loaded with the force F, the Young's modulus can be obtained as

$$E = \frac{\sigma}{\varepsilon} \quad \text{where} \quad \sigma = \frac{\mathrm{F}}{\mathrm{A_{CS}}} \tag{2.18}$$

and where ε is the axial strain.

Shear stiffness modulus G

For a member loaded in shear, the shear modulus can be obtained as

$$G = \frac{\tau}{\gamma} \tag{2.19}$$

where τ is the shear stress and γ the shear angle.

2.4.2 Cross-sectional area moment of inertia

The cross-sectional area moment of inertia I is a geometrical property that describes how the area of the cross-section is distributed with regard to an arbitrary axis. I is calculated as

$$I_X = \int y^2 dA, \quad I_Y = \int x^2 dA \tag{2.20}$$

where y is the perpendicular distance from the X-axis to the elemental area dA, similarly for x. For a thin walled cross-section, the moment of inertia from the center can be expressed as

$$I_{x/y} = \frac{\pi\, r^4}{4} - \frac{\pi\,(r-t)^4}{4} \tag{2.21}$$

whereby it is found that the cross-sectional area moment of inertia can be increased by either increasing the radius r or the wall thickness t.

2.5 Stability

Structures that are “slender” in the sense that at least one dimension is significantly smaller than the others are in general sensitive to the instability phenomenon known as buckling. Buckling occurs when the structure is loaded in compression and it is characterized by a large sudden deflection and often subsequent failure of the structure. This occurs even though the stresses may be well below the ultimate strength of the material. The buckling strength is thus not determined by the material strength but primarily by the stiffness of the structure.

One definition of stability can be stated as in [7]: “A state of static equilibrium is (statically) stable, if a small change of the load will imply only a small change of the configuration (displacements) of the structure. Conversely, if such a small change of the load leads to large configuration changes, then the equilibrium is unstable”.

A ski pole is loaded by an off-center axial force via the strap attached to the handle. This induces axial loading and bending moment causing the structure to be in risk of reaching an unstable state. For small loads, the relation between the applied load and the deflection is linear but for larger loads the relation becomes non-linear. As the loading approaches the maximum carrying capability of the structure, the deflection approaches an horizontal asymptote, see Figure 2.5. This means that it, by above mentioned definition, approaches an unstable state.

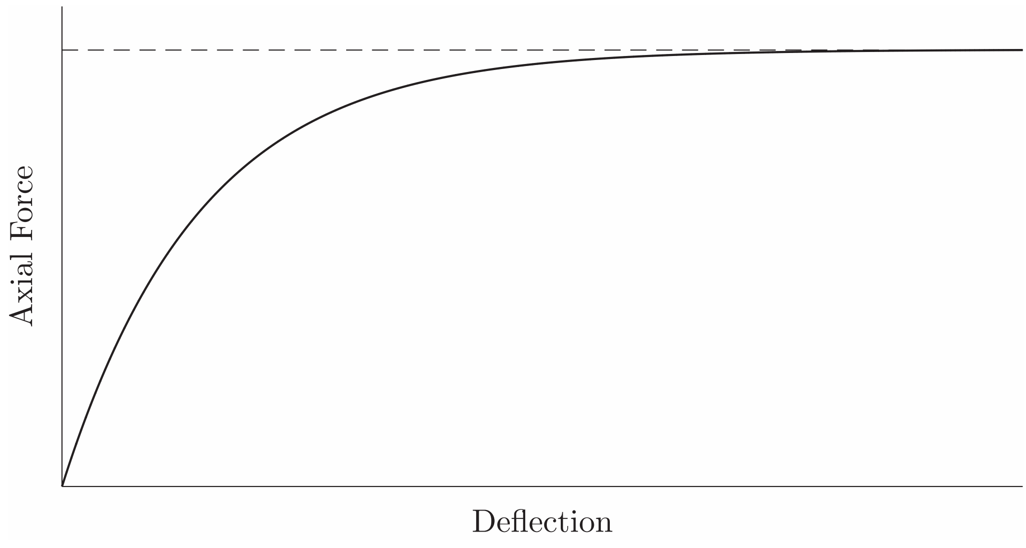

Figure 2.5: *Example of load deflection curve approaching a horizontal asymptote*

2.6 Quasi-static response

An impact will in general initiate elastic waves that propagate from the impact point. Depending on the impact duration, these waves will be dominated by different responses. For short impact times, the response is dominated by three dimensional wave propagation or flexural waves and shear waves. However, if the impact time is longer than the time that it takes for the waves to reach the boundary the response is dominated by the lowest mode of vibration. This response is quasi-static as the deflection and the load have the same relation as in the static case [8], which has been used for all impacts during this thesis.

3 Methods

To efficiently generate and evaluate new ski pole concepts, two parameterized FE models had to be developed to objectively determine and quantify the performance. The models used to evaluate the concept performance were a full scale bending test and a three point bending test. Each model was calibrated using experiments to ensure accuracy. Complementary to these tests; experiments to determine elastic modulus, shear modulus, max stress and max strain were done to obtain input data for the FE models. Details on the models and the experiments are described in this chapter.

Prior to project starting, a number of *Skigo Race 2.0* ski poles had been acquired. During the course of the project it turned out that Skigo had changed supplier, consequently the analysis was extended to include a comparison between the ski poles from the old and the new supplier. In this report, these ski poles will be referred to as the “new ski pole” and the “old ski pole”.

3.1 Ski pole geometry evaluation

For the FE analysis of the full scale bending test, an accurate Computer aided design (CAD) model of the old and the new ski pole was created. This CAD model was built using CATIA V5 [9]. In order to get the correct dimensions, the ski poles cross-sections were incrementally measured with calipers and advanced image analysis. In the image analysis, scanned cross-sections were processed by two different methods. In this report, these methods are referred to as; the *Matlab method* and the *Catia method*. Figure 3.1 shows processed images using the two different methods.

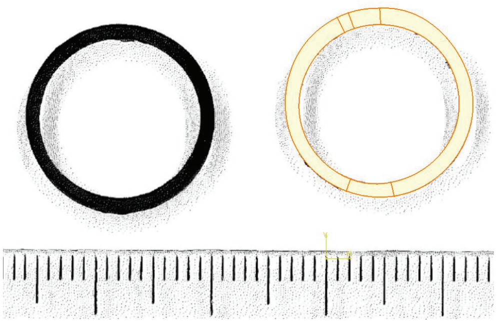

(a) *Left: scanned cross-section, Right: sketched surface on cross-section using the Ccatia method*

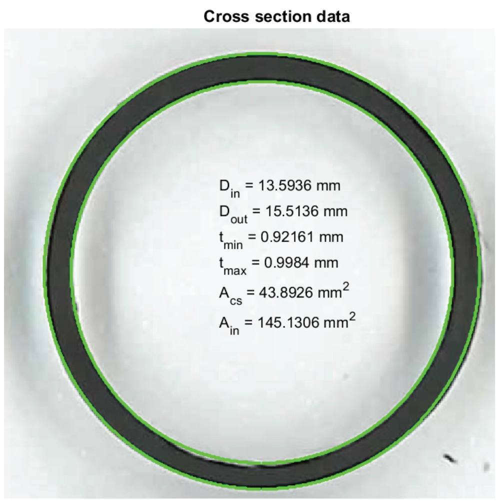

(b) *Cross-section analyzed with the Matlab method*

Figure 3.1: *Analyzed cross-sections*

The method of choice was dependent on the roundness of the cross-section. The *Matlab method* uses a MATLAB [10] script, see Appendix B, where a Hough transform [11] was used to identify circular shapes. The geometrical properties could then be obtained from the identified outlines, see green circles in Figure 3.1b. This method showed high efficiency but suffered from inaccuracy when the cross-sections deviate from an ideal circular shape.

In such cases, the *Catia method* was utilized. This method was more tedious since it required manual identification of the cross-section edges. A scanned cross-section was imported to CATIA V5 [9] and a sketch of the cross-section outlines was made manually. Generating a surface between the outlines enabled CATIA V5 to compute the desired geometrical dimensions using a measuring function, see Figure 3.1a.

The image analysis yielded the following geometrical dimensions; inner diameter D_{in}, outer diameter D_{out}, thinnest wall thickness $t_{\min}$, thickest wall thickness $t_{\max}$, inner area A_{in} and cross-sectional area A_{CS}.

3.2 Characterization of material properties

From the aforementioned bachelor's thesis [1], the fiber lay-up, volume fraction of fibers and matrix had been procured for the old ski pole. Since the ski pole analysis in this thesis includes the old and the new ski pole it was decided to redo the analysis on the old ski pole for the relative comparison to be accurate. Thus, both the new and the old ski pole were analyzed for laminate lay-up, volume fractions of fibers, matrix and voids in different laminas and laminate stiffness and strength. In particular, the longitudinal modulus E_{L}, the in-plane shear modulus G_{LT} and the compressive strength σ'_{LU} could be determined from tensile, torsional and compressive tests.

The data from the experiments required a transformation from global coordinates to the local fiber oriented system. The resulting equation is presented in Equation (3.3) and were stated under the assumption that each lamina contributes to the global stiffness proportional to their thickness. Thus, for the old pole, which had fibers in the 0° and in 45°, the global stiffness was stated as

$$\overline{\boldsymbol{Q}}_{\mathrm{global}} = \frac{t_{0^\circ}}{t_{\mathrm{tot}}}\overline{\boldsymbol{Q}}_{0^\circ} + \frac{t_{45^\circ}}{t_{\mathrm{tot}}}\overline{\boldsymbol{Q}}_{45^\circ}. \tag{3.1}$$

For the new pole, the corresponding equation was

$$\overline{\boldsymbol{Q}}_{\mathrm{global}} = \frac{t_{0^\circ}}{t_{\mathrm{tot}}}\overline{\boldsymbol{Q}}_{0^\circ} + \frac{t_{90^\circ}}{t_{\mathrm{tot}}}\overline{\boldsymbol{Q}}_{90^\circ}. \tag{3.2}$$

By only considering the in-plane components of the stiffness matrix $\overline{\boldsymbol{Q}}$, expressions for the longitudinal stiffness modulus and the in-plane shear modulus could be stated as

$$\begin{bmatrix} E_{\mathrm{z}} \\ G_{\mathrm{z}\varphi} \end{bmatrix} = \boldsymbol{A}\begin{bmatrix} E_{\mathrm{L}} \\ G_{\mathrm{LT}} \end{bmatrix} + \boldsymbol{b}E_{\mathrm{T}} \Rightarrow \begin{bmatrix} E_{\mathrm{L}} \\ G_{\mathrm{LT}} \end{bmatrix} = \boldsymbol{A}^{-1}\left(\begin{bmatrix} E_{\mathrm{z}} \\ G_{\mathrm{z}\varphi} \end{bmatrix} - \boldsymbol{b}E_{\mathrm{T}}\right). \tag{3.3}$$

Where $\boldsymbol{A}$ is a 2×2 coefficient matrix, with coefficients depending on the lay-up, and $\boldsymbol{b}$ is a 2×1 vector with coefficients to account for the transverse stiffness which was assumed to be known.

To ensure that the results would be representative for the pole as a whole, samples were taken from the cylindrical part (See Section 4.1) of the ski pole offset 100 mm to the edge of the handle. In Figure 3.2 the sequence of sample extraction can be seen. First a sample for tensile and torsion testing was extracted followed by a 5 mm sample for microscopy and last a sample for compression testing. To determine the cross-sectional area for the tensile and torsion test samples, thin specimens from the samples were cut after testing. The cross-sectional area of the compression test samples were considered to be the same as for the microscopy, since they were extracted in sequence. This assumption was made since the compression tests suffered from large deformations after testing whereby cutting in half and measuring would not yield accurate results. The cross-sections were analyzed using the methods described in Section 3.1.

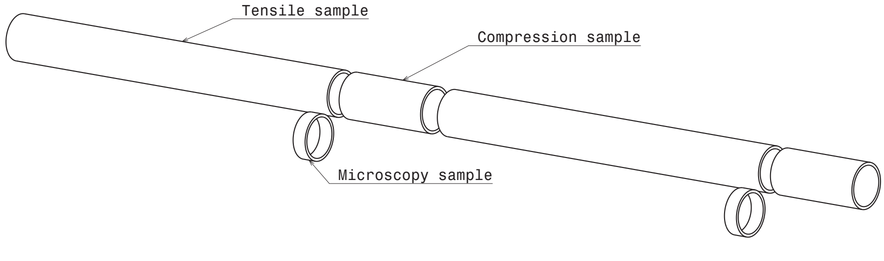

Figure 3.2: *Sample extraction form ski pole*

3.2.1 Tensile and shear testing

Tests were conducted using an MTS 809 Axial/Torsional Test System. A biaxial extensometer from MTS was used to measure torsion angle and tensile strains. The test was setup and recorded using MTS TestSuite.

To install the samples in the tensile testing machine, steel inserts were manufactured and glued to the specimens with *Adekit a140* epoxy glue [12], see Figure 3.3. The glue was hardened in accordance with the manufacturers recommendations with a radial gap of 0.2 mm, see Figure 3.4. The specified strength of the glue bond was 30 MPa. With only a limited number of ski poles available for testing, the specimen length was to be kept to a minimum. In order for the test to capture the ultimate tensile stress, the insert depth was needed to be about 70 mm. Whereby, theoretically, the glue would hold for a 1505 MPa stress could be transfered. That would have been sufficiently high to capture the expected ultimate tensile strength of a high performance CFRP. However, with the limitation on the amount of ski poles available, excluding the testing of the ultimate tensile stress would enable testing of more samples. Also, depending on the composite properties, the load limit could be the circumferential strength of the pole. Since the inserts prohibits circumferential contraction due to Poisson's effect the poles risk to fail from transverse stresses rather than the sought longitudinal stresses. Shortening the insert depth to 40 mm would theoretically enable testing of more samples up to 860 MPa, sufficient for determining in the tensile and shear stiffness. With the 40 mm insert, a specimen length of 134 mm was sufficient. Note that no particular standard was found suitable for the testing, rather the testing relied on the experience of supervisors and assistants.

Figure 3.3: *Tensile and torsion insert assembly*

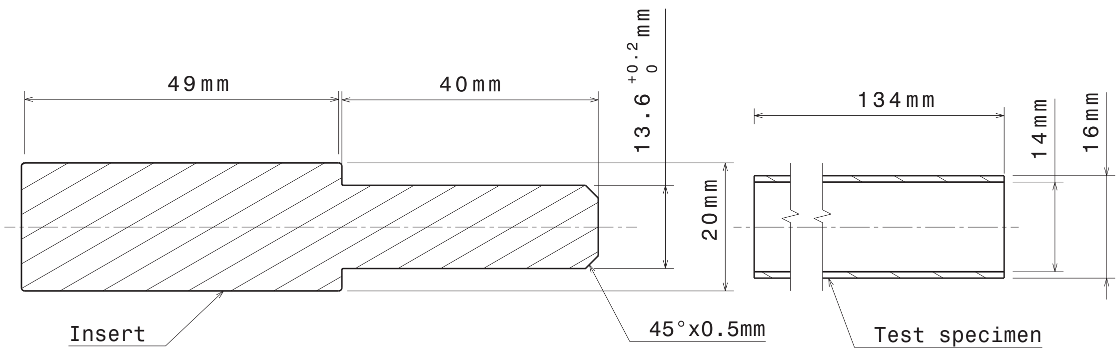

Figure 3.4: *Tensile and torsion insert assembly drawing*

Since the testing would only be conducted for the linear region, several load cycles could be applied to get more accurate results. Thereby a four step loading cycle routine was programmed to the tensile testing machine. First, a tensile load of 10 kN was applied twice, followed by a ±15 kN mm torsional load, also applied twice. Subsequent steps were a 10 kN tensile load followed by a 5 kN compressive load. This was not intended to contribute to the collection of stiffness data, but rather to verify that the tensile and torsion tests could be done in sequence yielding independent results. Since this was the case, data for four tensile and torsion cycles could be collected. As a final step the machine was set to apply displacement until failure.

To measure the axial strain ε and the torsion angle θ, a biaxial extensometer was used. The extensometer had to be modified in order to fit a test specimen with an outer diameter of 16 mm since this specific diameter was not supported. A new spacer was manufactured much alike the existing one but with necessary modifications. To ensure that this modification would not alter the accuracy of the extensometer, the new spacer was first tested on a 16 mm steel test specimen. By running another test with a 10 mm sample using a unmodified extensometer on the same material, it could be verified that the modification did not alter the accuracy of the measurements.

From the tensile test, the axial load and strains were obtained. The load was then used to calculate the stress

$$\sigma_{\mathrm{Z}} = \frac{F}{A_{\mathrm{CS}}} \tag{3.4}$$

which then was used to produce a stress-strain curve from which the stiffness could be obtained as the slope via

$$\sigma_{\mathrm{Z}} = E_{\mathrm{z}}\varepsilon. \tag{3.5}$$

From the torsion test, the applied torque and the shear angle were obtained. The in-plane shear modulus could then be calculated via the relation

$$\theta = \frac{TL}{G_{\mathrm{Z}\varphi}K} \tag{3.6}$$

where T is the applied torque, L is the length of the specimen, $G_{\mathrm{Z}\varphi}$ is the in-plane shear modulus and K is the polar moment of inertia. The polar moment of inertia for a thin-walled cross-section was calculated as

$$K = \frac{4A_{\mathrm{in}}^2}{\oint \frac{ds}{t(s)}}, \tag{3.7}$$

with A_{in} being the inner area, $t(s)$ the wall thickness and s a coordinate along the mean circumference [6], see Figure 2.2.

3.2.2 Compressive testing

To determine the ultimate compressive strength σ'_{TU}, compressive tests were conducted. The testing was guided by the ASTM D5449 standard [13]. The standard suggests test specimens with a diameter of 140 mm and 100 mm in length. The ski pole has an outer diameter of 16 mm whereby scaling with the diameter yields a specimen length of 11.4 mm. Though, in order to fit strain gauges and compression fixtures the specimens were further extended to 34 mm.

In order to distribute the compressive load and to avoid crushing of the specimen ends, the standard suggests the use of fixtures. The fixtures were scaled in a similar manner yielding a fixture that can be seen in Figure 3.5. For securing the test specimen in the fixture and for removing cavities, the standard suggest to use a "potting material". For this, a hot-melt adhesive was used since it would provide a sufficient bond while enabling reuse of the fixtures. To ensure that the compressive load would distribute evenly on the loaded boundaries, these edges were ground perpendicular to the surface of the specimen.

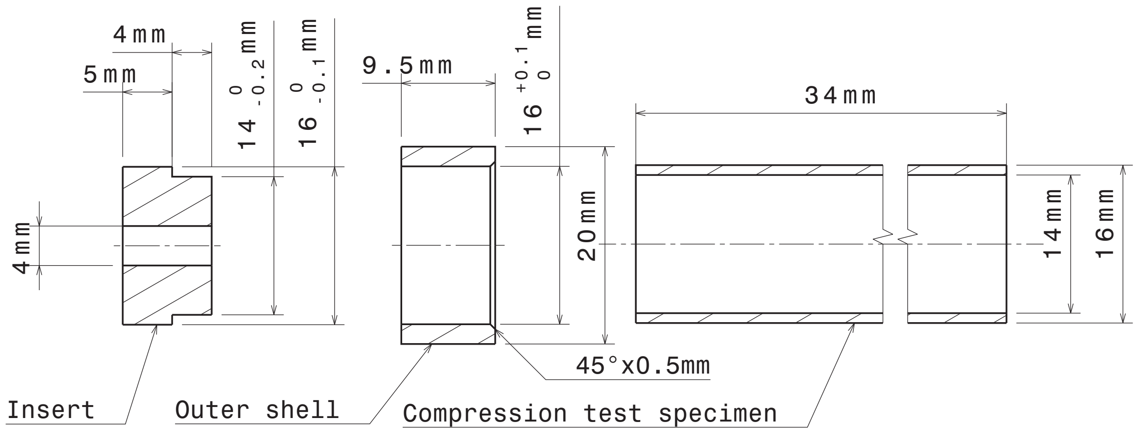

Figure 3.5: *Compression insert assembly*

For the compression testing, a INSTRON 4505 5500R test frame with a 100 kN load cell was used. To measure and record strains, equipment from LORD MICRO-MEASUREMENTS was used. Strains were measured using linear strain gauges (CEA-06-240UZ-120), the strain data was recorded using *Node Commander*. The force measured by the load cell was recorded using INSTRON *Blue Hill*.

3.2.3 Three point bend test

In order to evaluate any damage initialized by an impact, a three point bending test was performed under the assumption that the impact can be considered as a quasi-static event as described in Section 2.6. Specimens of length 230 mm were cut and loaded until failure by a rate of 1 mm/min.

The tests were conducted in the same machine as the compression test, but with a rig for three point bending as can be seen in Figure 3.6. The displacement was measured by the frame sensors. To obtain accurate results, the flexing of the machine had to be accounted for. The flexing of the machine was determined by allowing it to apply a compressive force directly to the bottom support. Subtracting these measurements from the actual testing gives the actual displacement of the specimen.

Figure 3.6: *Three point bending test setup*

3.2.4 Microscopy

In the microscope, the layup, the fiber area fraction, the fiber diameters as well as the void content were investigated. For each microscopy analysis, thin samples of the cross-section were cast in epoxy and then polished to a fine surface finish, Figure 3.7 shows a polished casting with three cross-sections. Details on the casting and polishing process is presented in Appendix A.

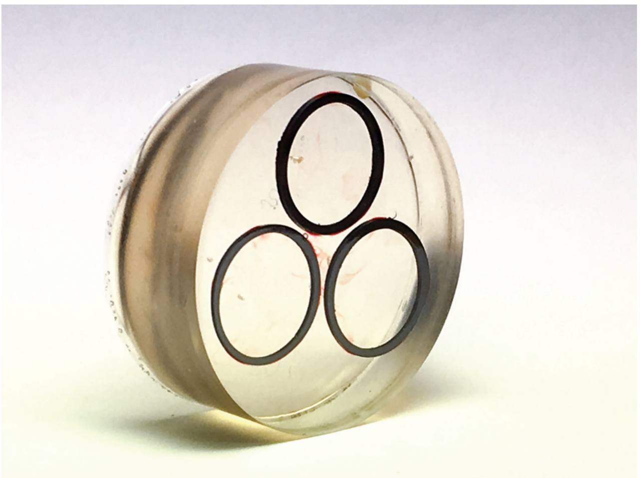

Figure 3.7: *Microscopy samples in epoxy casting*

From the microscopy, the fiber directions can be identified depending on the shape of the fibers cross-section. A circle would be a fiber normal to the cross-sectional surface. Elliptic shapes implies that the fiber is at an angle and the fibers appearing as white lines are parallel with the cross-section surface.

Lamina thicknesses was evaluated by image measurements. The area fraction of fibers, matrix and voids was measured using MATLAB, see Appendix D. In MATLAB, the images were transformed to a binary picture to differentiate between fibers, matrix and voids, see Figure 3.8. By this procedure, the area of fibers and the area of the voids could be determined. The area of the matrix was then given as the remaining area. The area fractions were calculated as

$$A_\mathrm{f} = \frac{a_\mathrm{f}}{a_\mathrm{c}} \tag{3.8}$$

$$A_\mathrm{m} = \frac{a_\mathrm{m}}{a_\mathrm{c}} = \frac{a_\mathrm{c} - a_\mathrm{v} - a_\mathrm{f}}{a_\mathrm{c}} = 1 - A_\mathrm{f} - A_\mathrm{v} \tag{3.9}$$

$$A_\mathrm{v} = \frac{a_\mathrm{v}}{a_\mathrm{c}} \tag{3.10}$$

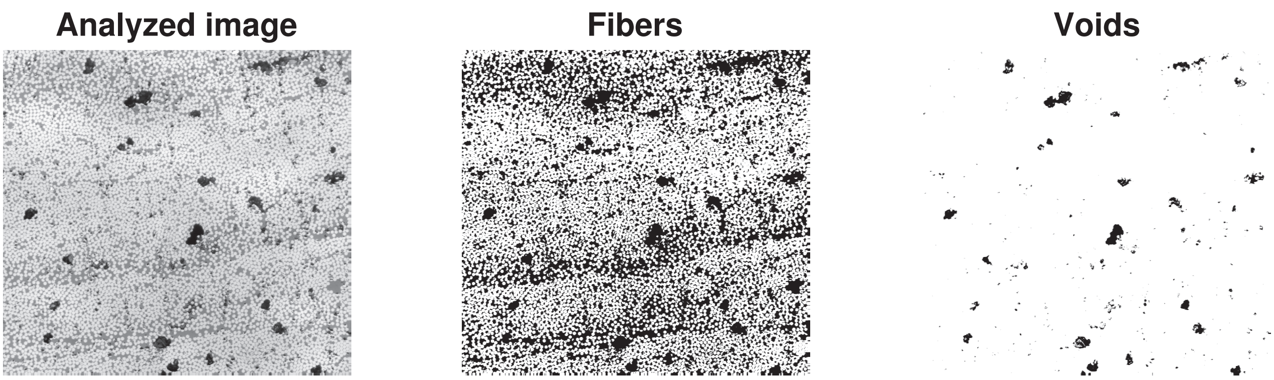

Figure 3.8: *Analyzed microscopy image showing the fibers and the voids of the CFRP*

The diameters of the fibers was also analyzed using a MATLAB script, see Appendix C. Figure 3.9 shows the output from this script where identified fibers are marked wit a green circle.

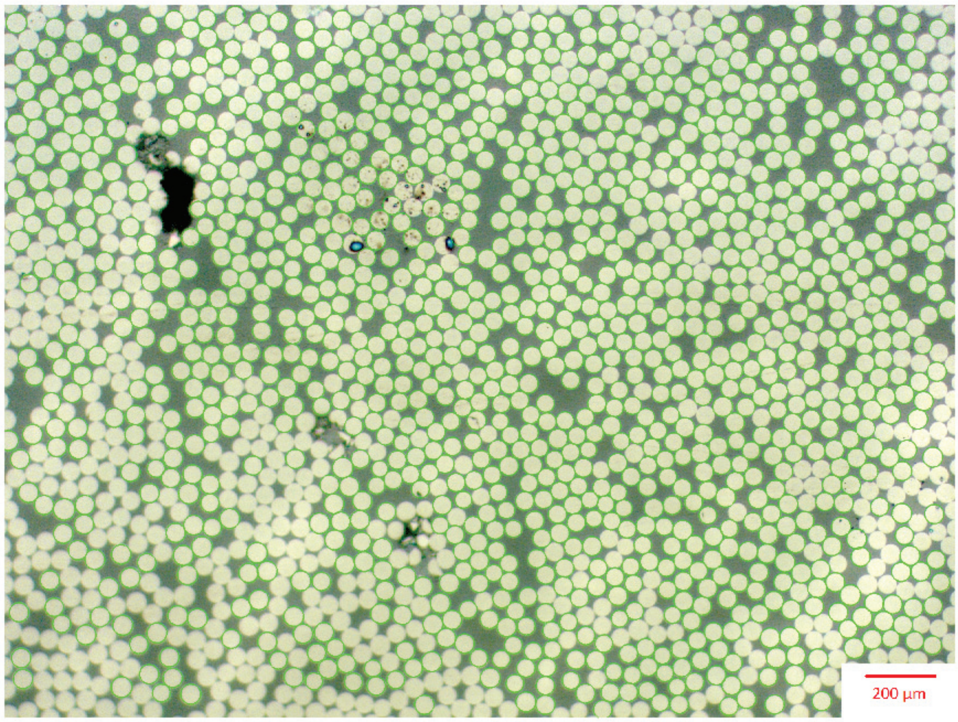

Figure 3.9: *Microscopy of the old ski pole, image analysis marks identified fibers with a green circle*

3.3 Numerical analysis

Two major FE models were developed; a full ski pole bending model and a three point bending model. The full scale bending FE model was built to capture the bending of the ski pole during usage whereas the three point bending FE model was to simulate the three point bending test as described in Section 3.2.3.

The FE analysis was done using the commercial software Ansys Mechanical. For pre-processing of the composite layup, Ansys Composite PrePost [14] (ACP) was used and for post-processing, ACP as well as Matlab [10] were used. The material was modeled as transversely isotropic using the material properties obtained from the experiments. Material properties that were not experimentally retrieved were estimated from tables in [15]. Details are presented in Tables 3.1 and 3.2.

Table 3.1: *Material data used in FE analysis, stiffnesses in* GPa

	E_{L}^{*}	E_{T}	$E_{\mathrm{T'}}$	ν_{LT}	ν_{TT}	$\nu_{\mathrm{TT'}}$	G_{LT}^{*}	$G_{\mathrm{TT'}}$	$G_{\mathrm{LT'}}$
Old ski pole	146.1	9.65	9.65	0.30	0.34	0.30	4.3	2.15	4.3
New ski pole	150.5	9.65	9.65	0.30	0.34	0.30	4.7	2.35	4.7

* *indicates experimentally obtained value*

Table 3.2: *Stresses used for damage initiation in* MPa

	σ_{LU}	$\sigma_{\mathrm{LU}}^{\prime *}$	σ_{TU}	$\sigma_{\mathrm{TU}}^{\prime}$	$\sigma_{\mathrm{T'U}}$	$\sigma_{\mathrm{T'U}}^{\prime}$	τ_{LTU}	$\tau_{\mathrm{TT'U}}$	$\tau_{\mathrm{LT'U}}$
Old ski pole	1314	616.5	43	168	43	168	48	32	48
New ski pole	1314	931.0	43	168	43	168	48	32	48

* *indicates experimentally obtained value*

The composite was modeled using classical laminate theory, i.e. the material is modeled as an orthotropic homogeneous material with the in-plane elastic properties varying through the thickness as described in Section 2.1.1. The following assumptions were made for the analysis:

- Fibers are uniformly distributed.
- Matrix is free of voids.
- Fiber and matrix is perfectly bonded.
- No residual stresses are present.
- Fibers and matrix behave linearly elastic.

The composite lay-ups were created using the functionality of the ACP module. The lay-ups for the old an new ski pole are presented in Table 4.1.

Large deformation formulation[1]was adopted to capture the non linear behavior that was expected in both the full scale bending test and the three point bending test.

[1]Large deformation theory implicates that the equilibrium equations are stated in the deformed geometry and updated with the deformation [16]

3.3.1 Full scale bending test

Prior to the project, Skigo had also performed full scale bending tests on the old ski pole which was used as reference to the FE model. In the full scale bending test, the loading was applied via the hand strap. By attaching it to a sled that moved on tracks in the longitudinal direction of the pole, see Figure 3.10. The tip of the ski pole was attached to a ball joint allowing free rotation. From the test the applied force and the maximum deflection was obtained.

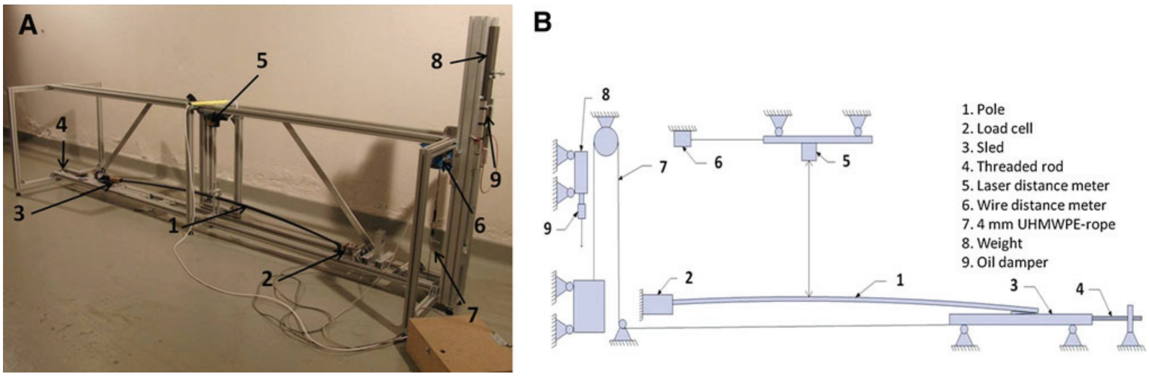

Figure 3.10: *Ski pole test rig, picture from [17].* ***A****: The pole is attached in the rig and subjected to an axial force.* ***B****: Schematic of the test rig*

Loading and boundary conditions

The boundary conditions for the full bending simulation were set to represent the setup of the tests performed previously by Skigo. In order to obtain accurate boundary conditions for the loading, the handle was incorporated as a solid part of a polymer material, see Figure 3.11. A drawing of the handle with loading point, support point and contact area can be seen in Figure 3.12. The contact between the pole and the handle was modeled as bonded since it is in reality bonded with hot-melt adhesive.

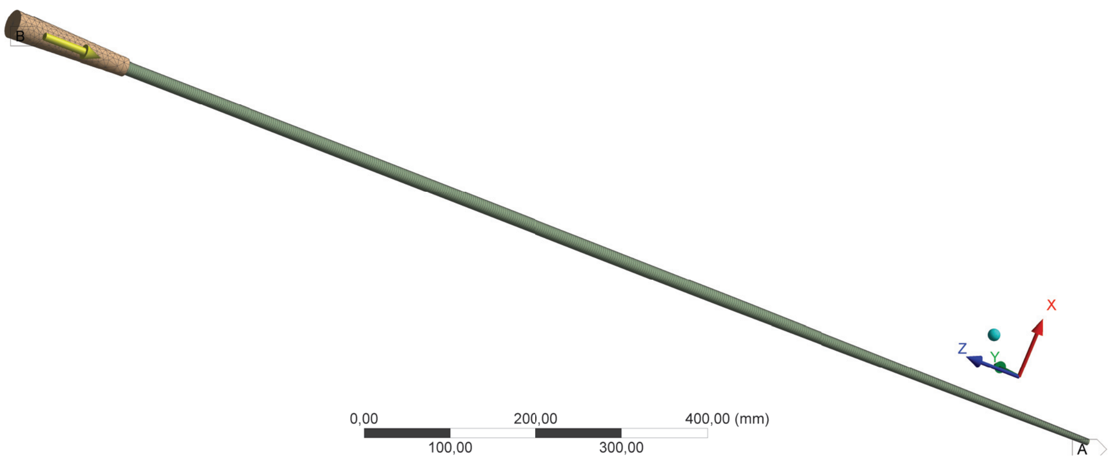

Figure 3.11: *FE model of ski pole as an assembly of pole and handle*

In the test rig the ski pole is pulled by the strap in the direction of the ski pole. This strap rests on a sled that is only allowed to move longitudinal to the ski pole (Z-direction). In the FE model this sled is modeled as a support point, and similarly to the sled, this point allows only for rotation around the X-axis and the translation in the Z-direction. The strap was modeled as a beam connecting the support point and the loading point. By moving the support point, the reaction forces at the loading point could be calculated, whereby the applied load on the strap was obtained. The total bending of the pole was taken as the maximum displacement in the Y-direction. The position for the loading point was at (0,1.75,1475) mm and the support point was located at (0,-19.781,1456.6) mm in global coordinates.

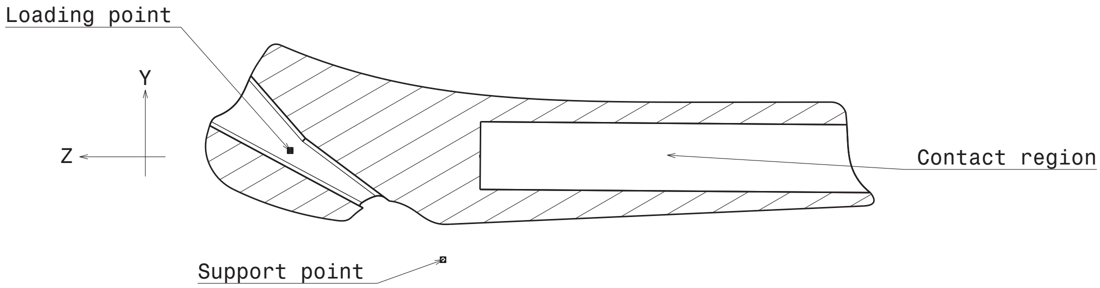

Figure 3.12: *Schematic sketch of a handle cross-section*

Mesh and element types

The full scale model of the pole was simulated using shell elements. More specifically, the ANSYS *SHELL181* element was used. It is a four node element governed by first order shear deformation theory [18].

For the model, 9568 elements were used. To ensure that the FE-mesh would be accurate, a mesh convergence study was done. The result can be seen in Figure 3.13.

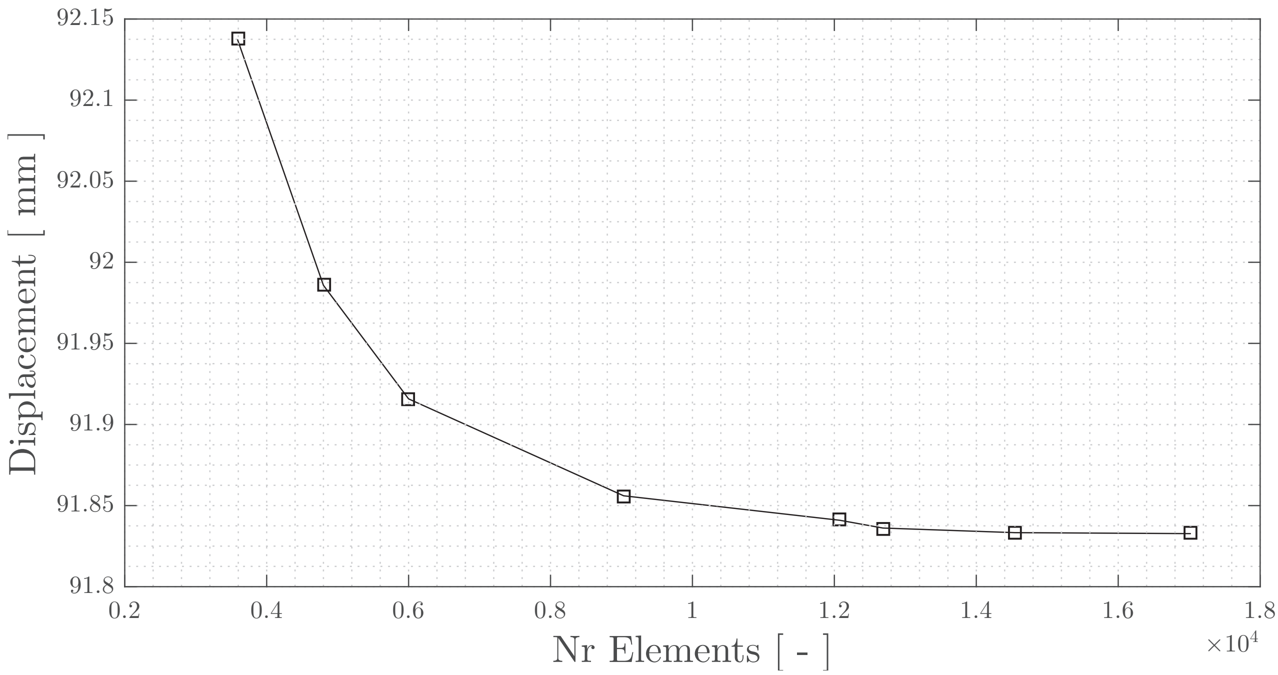

Figure 3.13: *Mesh convergence for full scale bending test using SHELL181 elements*

3.3.2 Three point bending

The three point bending simulation consisted of the pole sample supported by two steel cylinders at each end. The loading was applied by a third steel cylinder at the middle of the span, see Figure 3.6. To reduce the computational time, symmetry was utilized and thus only half of the assembly was analyzed in the FE analysis, see Figure 3.14. The old ski pole has one 45° layer which makes the structure asymmetric around the midpoint. To save computational time, this asymmetry was neglected in the analysis since this layer does not significantly contribute to the bending stiffness.

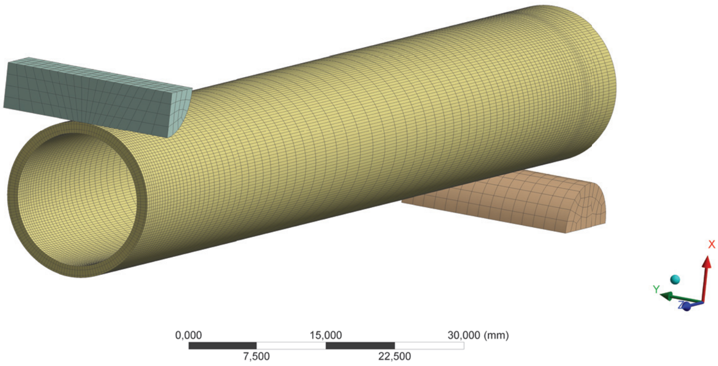

Figure 3.14: *Symmetry model of the three point bending FE model*

The supporting cylinders were set as fixed and the loading was carried out by a prescribed displacement of the top cylinder. In order to further simplify the analysis the contact between the cylinders and the pole was set as frictionless.

Damage modeling

Modeling of damage of the composite in Ansys required two inputs; a damage initiation criteria and a damage evolution law. To predict initial damage the Hashin failure criterion was used since it did not require any additional material parameters except the ultimate stress. The failure criteria also takes load interaction in consideration and have an criteria for delamination.

Progressive damage was modeled using a Material Property Degradation (MPDG) model where the stiffness of an element is instantly reduced by a predefined factor when a failure criterion has been triggered, see Section 2.3. The failure criteria considered in the MPDG model were longitudinal tensile failure, longitudinal compressive failure, transverse tensile failure and transverse compressive failure which each had its own degradation factor. Due to the difficulty in estimating the degradation factor several values were used and compared, the factors used can be seen in Table 3.3.

Table 3.3: *Degradation factors used in the different simulations*

	Degradation factors			
	Fiber tensile	Fiber compression	Matrix tensile	Matrix compression
Simulation 1	0.5	0.5	0.5	0.5
Simulation 2	0.65	0.65	0.65	0.65
Simulation 3	0.8	0.8	0.8	0.8
Simulation 4	0.99	0.99	0.65	0.65

3.4 Modeling of concept ski poles

The boundary conditions for the concept model pole were identical to those used for the reference ski poles. However, for the three point bending test of the foam core concept, 3 solid elements were used through the thickness. This would more accurately capture the shear deformation of the core as well as the through-thickness stresses. The solid-shell element used was the *SOLSH190* which is used to simulate shell structures but features a continuum solid element topology with eight nodes. Using solid elements increased the number of element required. For this model 30.000 elements were used.

4 Results

4.1 Reference ski pole geometry

In Figure 4.1, the measured outer diameters from the reference ski pole can be seen. The ski pole design is a cylindrical tube with a tapering starting at 600 mm measured from the tip. The old ski pole has a smaller diameter than the new ski pole in the tapered region. For the cylindrical part, both ski poles have an average diameter of 16 mm.

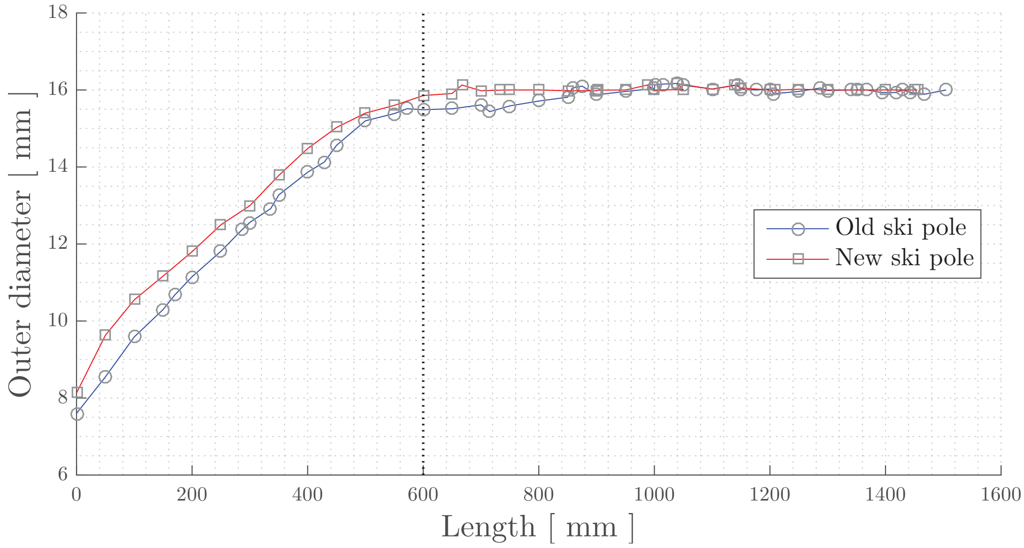

Figure 4.1: *Measured diameters of old and new Race 2.0 ski poles*

It was found that the ski poles have a consistent thickness through the length, apart from the slightly thinner wall thicknesses close to the edges, see Figure 4.2. Excluding the edges, an average laminate thickness is calculated to 0.99 mm for the old ski pole and 1.00 mm for the new ski pole. The old ski pole has a larger scatter.

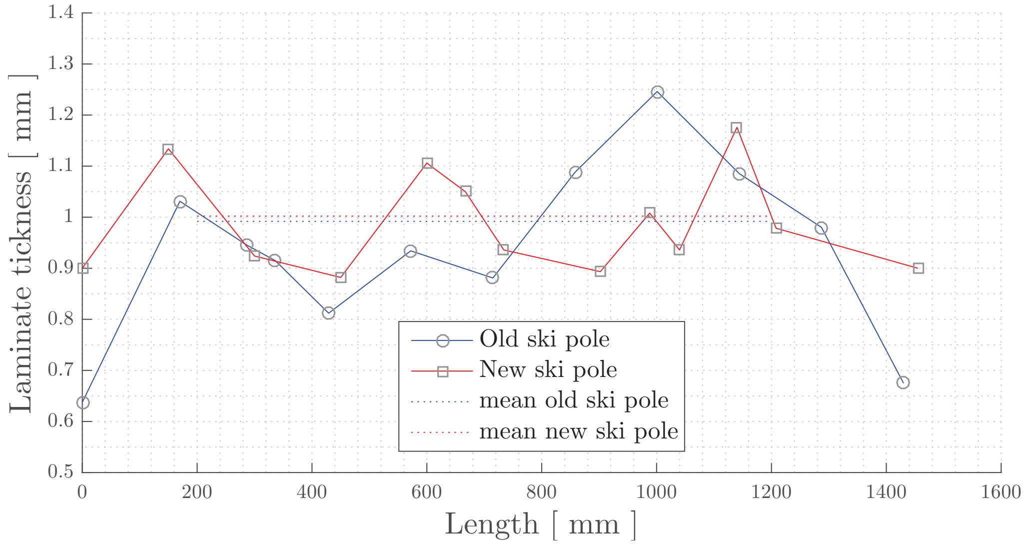

Figure 4.2: *Measured laminate thickness of old and new Race 2.0 ski poles*

4.2 Composite lay-up

In the microscopy analysis, it was found that the old ski pole and the new ski pole have different lay-ups. The old ski pole has a lay-up of $[0_5/45]$, that can be seen in Figure 4.3, whereas the new pole has a lay-up of $[0_2/90/0/90/0_2/90]$, that can be seen in Figure 4.4a. The lamina orientations and thicknesses are summarized in Table 4.1.

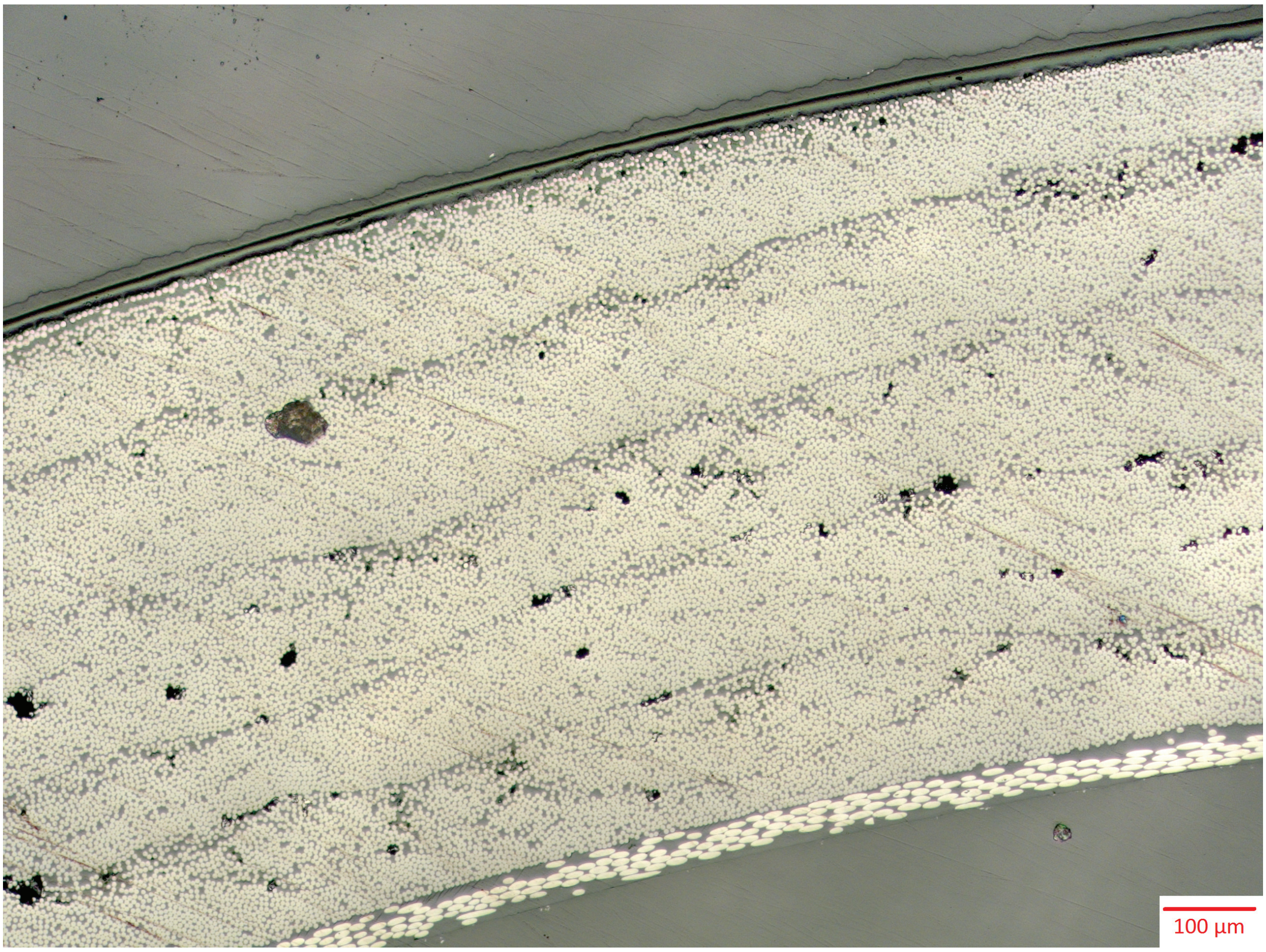

Figure 4.3: *Fiber lay-up in the old ski pole, seen from the r-φ plane in local coordinates*

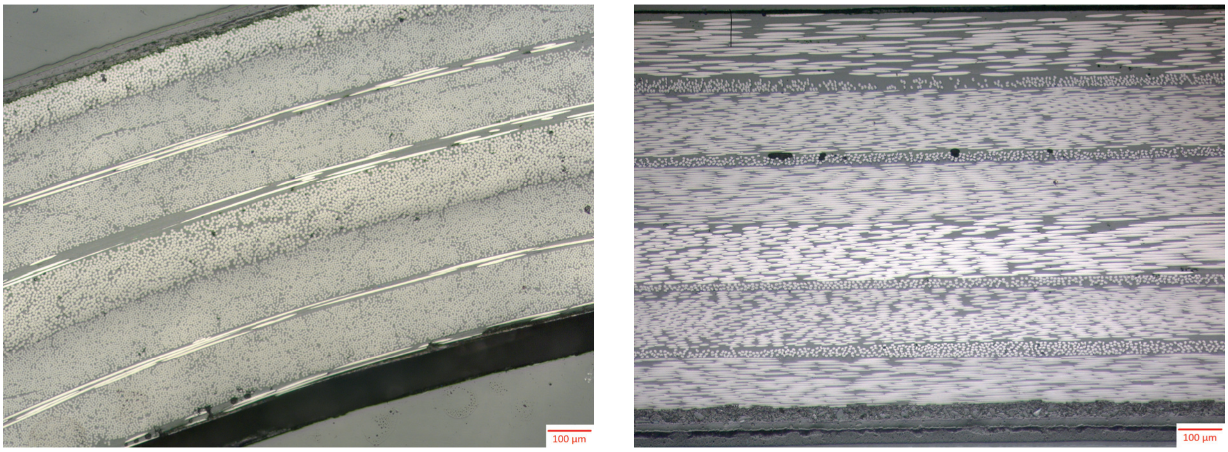

(a) *Seen from the r-φ plane in local coordinates* (b) *Seen from the $r - z$ plane in local coordinates*

Figure 4.4: *Microscopy of lay-ups for the new ski pole*

Table 4.1: *Lay-up properties of old and new ski poles*

	Old ski pole		New ski pole	
	Orientation [°]	Thickness [µm]	Orientation [°]	Thickness [µm]
Lamina				
1	45	67	90	26
2	0	174	0	143
3	0	168	0	148
4	0	169	90	23
5	0	168	0	139
6	0	211	90	31
7			0	112
8			0	136
9			90	31
10			0	124
11			90	25
12			0	64
Total thickness		956		1010

The average thickness for the 0° laminas in the old ski pole were 178 µm and 67 µm for the 45° laminas. For the new ski pole the average thickness of the 0° were 124 µm and 27 µm for the 90° laminas. These average thicknesses were used in the FE model.

4.3 Laminate properties

Figure 3.9 shows an image of the 0° fibers of the old ski pole. The fiber diameter was found to be 5.46 µm.

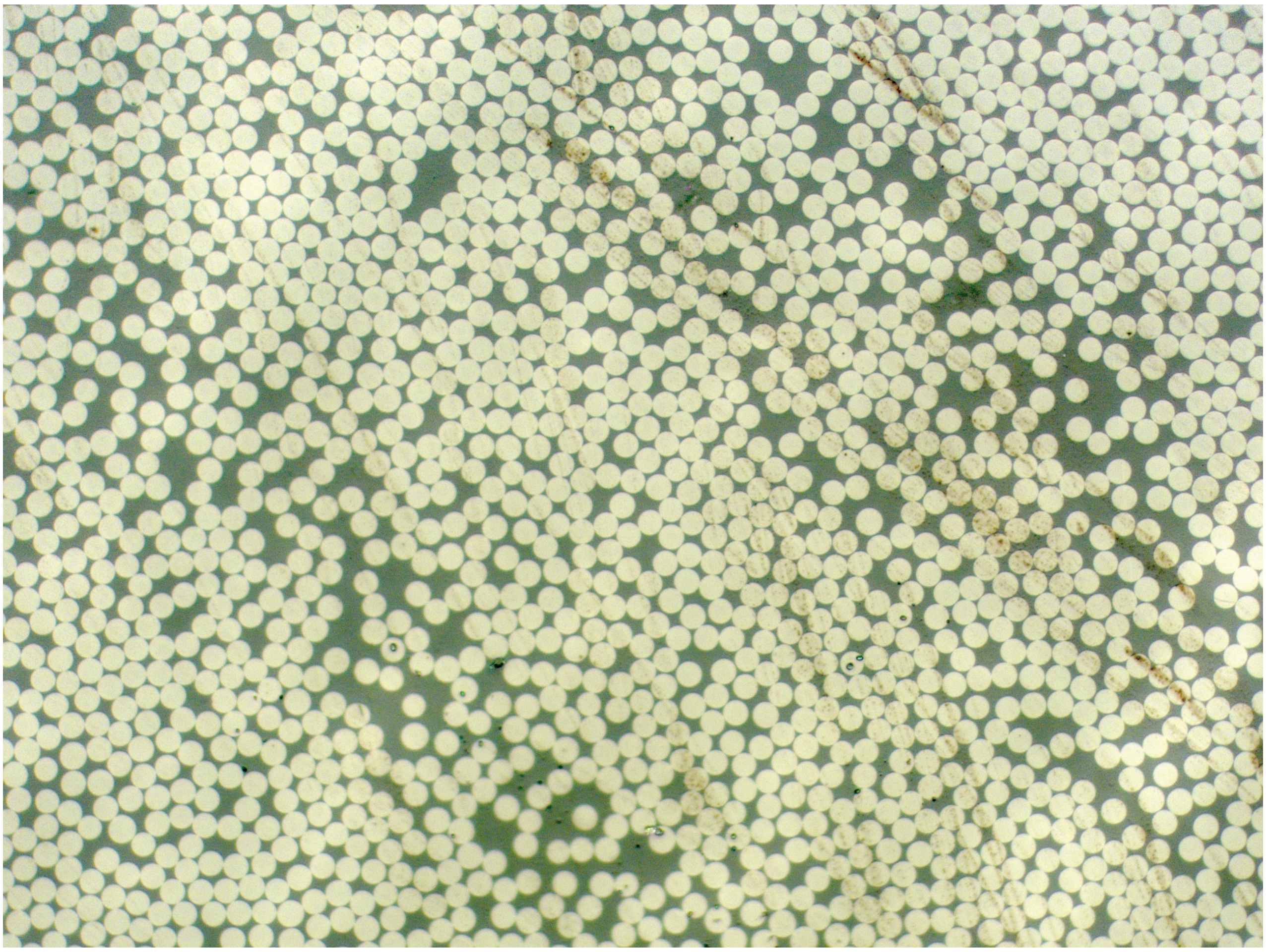

Figure 4.5: *Microscopy image of the longitudinal fibers of the old ski pole*

In Table 4.2, the area fraction of fibers, matrix and voids are presented for the old ski pole.

Table 4.2: *Area fraction of fiber, matrix and void for old pole*

	Old ski pole		
	fiber [%]	matrix [%]	void [%]
mean value	68.27	31.00	0.73
standard deviation	3.26	3.02	0.73
coefficient of variation	4.77	9.75	99.74

For the new ski pole, there were fibers with two different diameters identified from the microscopy analysis, see Figure 4.6. Image analysis concluded that there were larger fibers with average diameter of 7.1 µm, Figure 4.6b, and smaller fibers with average diameter of 5.5 µm, Figure 4.6a. It can also be observed that the larger fibers have a rounded grain shape as opposed to the smaller fibers with a circular shape.

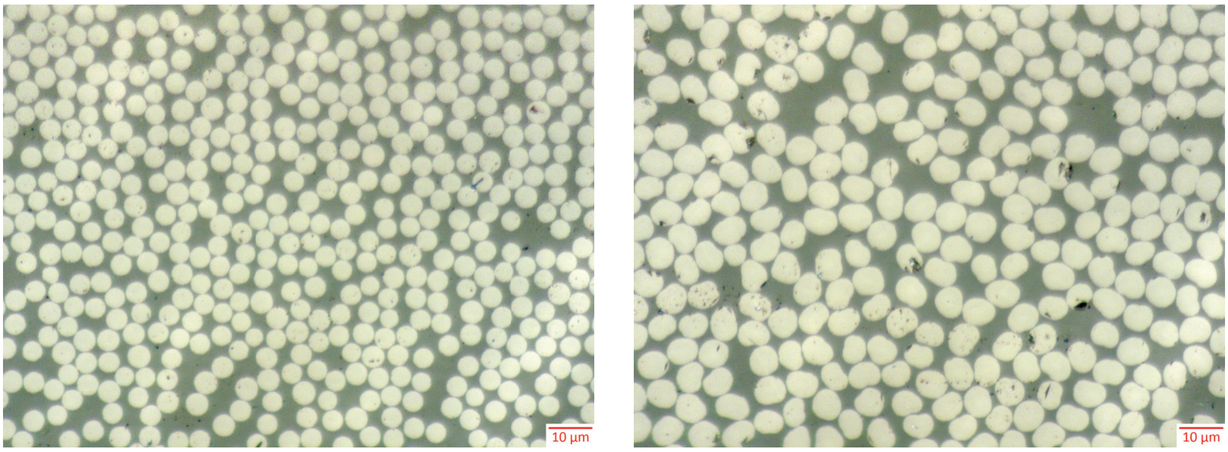

(a) *Small fibers* (b) *Large fibers*

Figure 4.6: *Different sized fibers in the new pole.*

The area fractions for the new pole were analyzed for the two types of laminates that were identified in Figure 4.6. The results are presented in Table 4.3

Table 4.3: *Area fraction of fiber, matrix and void for new pole*

	New ski pole (small fibers)			New ski pole (large fibers)		
	fiber [%]	matrix [%]	void [%]	fiber [%]	matrix [%]	void [%]
mean value	64.2	35.8	0.02	55.6	44.3	0.06
standard deviation	3.4	3.4	0.02	6.9	6.9	0.06
coefficient of variation	5.3	9.6	117.7	12.4	15.6	104.09

4.4 Material properties characterization

In order to calculate the stiffness modulus from the measured global laminate stiffness, an equation was derived, as presented in Equation 3.3. It was derived using the assumptions regarding the global stiffness described in Equation 3.1 and 3.2. The resulting equation for for the old and the new ski pole becomes

$$\begin{bmatrix} E_\mathrm{z} \\ G_{\mathrm{z}\varphi} \end{bmatrix} \approx \begin{bmatrix} 0.947 & 0.070 \\ 0.018 & 0.930 \end{bmatrix} \begin{bmatrix} E_\mathrm{L} \\ G_\mathrm{LT} \end{bmatrix} + \begin{bmatrix} 0.028 \\ 0.07 \end{bmatrix} E_\mathrm{T} \tag{4.1}$$

and

$$\begin{bmatrix} E_\mathrm{z} \\ G_{\mathrm{z}\varphi} \end{bmatrix} \approx \begin{bmatrix} 0.864 & 0 \\ 0 & 1 \end{bmatrix} \begin{bmatrix} E_\mathrm{L} \\ G_\mathrm{LT} \end{bmatrix} + \begin{bmatrix} 0.136 \\ 0 \end{bmatrix} E_\mathrm{T} \tag{4.2}$$

respectivly.

4.4.1 Tensile and torsion test

In Tables 4.4 and 4.5, the experimental results for the old and new poles are presented, respectively. In each table the result for each test specimen per load cycle is presented with a calculated average.

Table 4.4: *Measured and recalculated values of longitudinal stiffness and in-plane shear stiffness of the old pole in* GPa

	Sample 1				Sample 2				Sample 3			
load cycle	E_z	E^*_L	$G_{\mathrm{z}\varphi}$	G^*_LT	E_z	E^*_L	$G_{\mathrm{z}\varphi}$	G^*_LT	E_z	E^*_L	$G^{**}_{\mathrm{z}\varphi}$	$G^{*/**}_\mathrm{LT}$
1	144.1	151.4	7.9	5.6	135.7	142.6	7.1	4.9	139.6	146.7	7.4	5.2
2	143.8	151.2	7.5	5.2	135.1	142.1	6.7	4.9	138.1	145.4	3.7	1.1
3	144.0	151.4	7.6	5.2	134.5	141.4	6.8	4.5	135.4	142.5	5.6	3.2
4	144.4	151.8	7.4	5.1	134.8	141.8	6.6	4.4	137.3	144.5	5.3	2.9
mean	144.1	151.5	7.6	5.3	135.0	141.9	6.8	4.6	137.6	144.8	5.5	3.1

** indicates calculated value, ** suspected partial failure*

Table 4.5: *Measured and recalculated values of longitudinal stiffness and in-plane shear stiffness of the new ski pole in* GPa

	Sample 1				Sample 2				Sample 3			
load cycle	E_z	E^*_L	$G_{\mathrm{z}\varphi}$	G^*_LT	E_z	E^*_L	$G_{\mathrm{z}\varphi}$	G^*_LT	E_z	E^*_L	$G_{\mathrm{z}\varphi}$	G^*_LT
1	129.0	147.8	4.4	4.4	123.9	141.9	4.9	4.9	145.9	167.4	5.2	5.2
2	128.8	147.5	4.4	4.4	124.3	142.4	4.6	4.6	141.8	162.6	5.3	5.3
3	128.5	147.2	4.3	4.3	119.9	137.3	4.6	4.6	140.1	160.6	5.2	5.2
4	128.9	147.7	4.2	4.2	123.1	141.0	4.5	4.5	142.3	163.1	5.1	5.1
mean	128.8	147.5	4.3	4.3	122.8	140.6	4.6	4.6	142.5	163.4	5.2	5.2

** indicates calculated value*

In Tables 4.6 and 4.7, the mean values of the results in Tables 4.4 and 4.5 are presented. The tables also present the lamina properties calculated using Equation (4.1) and Equation (4.2).

Table 4.6: *Overall mean stiffness, standard deviation and coefficient of variation of old ski pole*

	E_z	E_L^*	$G_{z\varphi}$	G_{LT}^*
mean value [GPa]	138.9	146.1	6.6	4.3
standard deviation [GPa]	4.1	4.3	1.2	1.3
coefficient of variation [%]	3.0	2.9	18.2	29.9

** indicates calculated value*

Table 4.7: *Overall mean stiffness, standard deviation and coefficient of variation of new ski pole*

	E_z	E_L^*	$G_{z\varphi}$	G_{LT}^*
mean value [GPa]	131.4	150.5	4.7	4.7
standard deviation [GPa]	8.8	10.2	0.4	0.4
coefficient of variation [%]	6.7	6.7	8.3	8.3

** indicates calculated value*

4.4.2 Compression test

Table 4.8 presents the experimental data for the two tested samples of each pole. The results are averaged between the tested samples and they are summarized in Table 4.9. The table also presents the lamina properties calculated using Equation (4.1) and Equation (4.2).

Table 4.8: *Results from compression tests*

	Sample 1				Sample 2			
	E_z [GPa]	E_L^* [GPa]	$\sigma_{LU}'^*$ [MPa]	ε_{zU}' [%]	E_z [GPa]	E_L^* [GPa]	$\sigma_{LU}'^*$ [MPa]	ε_{zU}' [%]
Old ski pole	92.2	96.7	547.8	0.57	116.3	122.2	685.11	0.56
New ski pole	136.6	156.6	985.1	0.65	144.8	166.1	876.3	0.52

** indicates calculated value*

Table 4.9: *Elastic modulus from compression tests*

	Old ski pole		New ski pole	
	E_z	E_L^*	E_z	E_L^*
mean value [GPa]	104.3	109.5	140.7	161.4
standard deviation [GPa]	17.1	18.0	5.8	6.7
coefficient of variation [%]	16.5	16.5	4.1	4.2

** indicates calculated value*

The maximum stress and strain obtained from experiments are presented in Tables 4.10 and 4.11.

Table 4.10: *Maximal longitudinal stress calculated from compression test results*

	Old ski pole	New ski pole
	σ'_{LU}	σ'_{LU}
mean value [MPa]	616.5	931.0
standard deviation [MPa]	97.1	77.5
coefficient of variation [%]	15.8	8.3

Table 4.11: *Maximum strain from compression tests*

	Old ski pole	New ski pole
	$\varepsilon'_{\mathrm{zU}}$	$\varepsilon'_{\mathrm{zU}}$
mean value [%]	0.57	0.59
standard deviation [%]	0.01	0.09
coefficient of variation [%]	1.8	15.3

4.5 Three point bending

Figure 4.7 shows the force-displacement plot of the experimental three point bending tests. All tests were stopped at 5 mm, this ensured that the ultimate failure would be captured on all specimens. The new ski pole is considered to have failed at 500 N/2.8 mm and the old ski pole is considered to have failed at 400 N/2.3 mm. However, the old ski pole still has some load carrying capacity after ultimate failure for some specimens but its behavior is unpredictable.

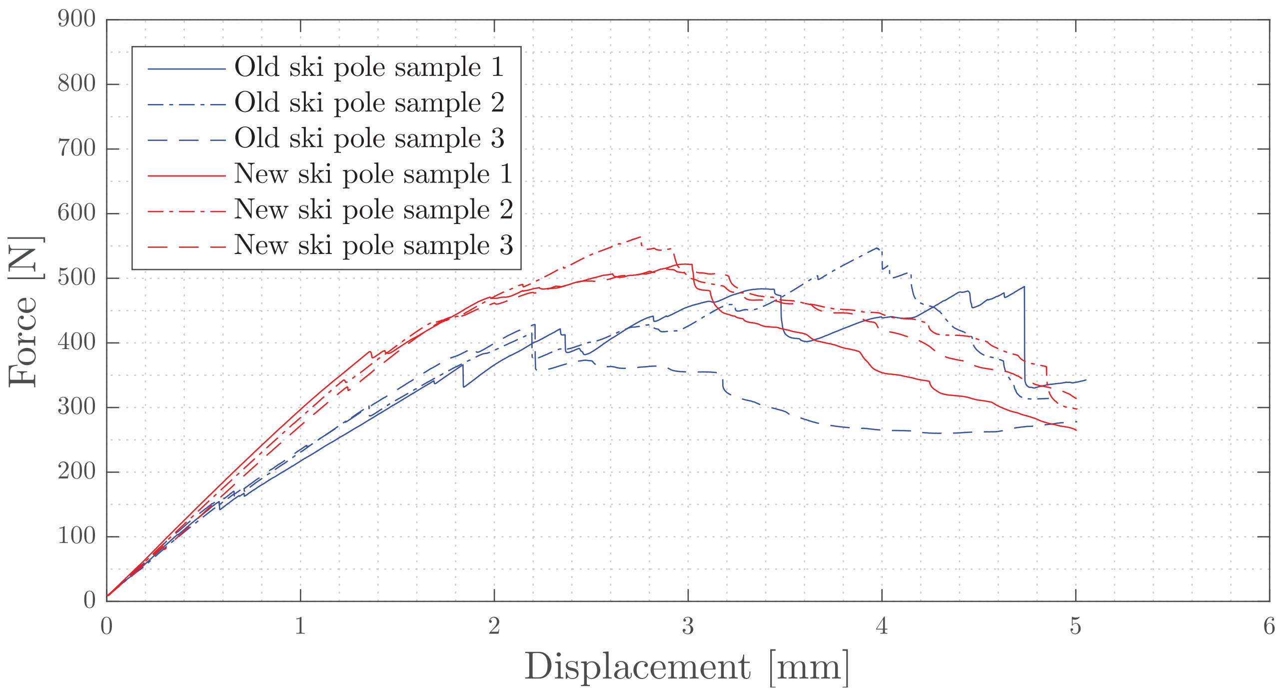

Figure 4.7: *Test data for three point bending test*

Figure 4.8 shows the visible cracks and crushing occurring at the loading point for the old ski pole and the new ski poles. For both the new and old ski poles the areas, where the load was applied, has been damaged. On the old ski pole, shown in Figure 4.8a, two longitudinal cracks can be seen, the upper one is on the point where the load was applied and the lower crack is one of the cracks that occurs symmetrically around the loading point.

On the new ski pole, no longitudinal cracks were found. The transverse cracks were more severe on the new ski pole than on the old ski pole reaching 90° from the loading point on each side. The transverse crack on the old ski pole is in between the longitudinal cracks and seems to be an effect from the crushing rather than a crack that has propagated.

(a) *Visible cracks on old ski pole* (b) *Visible cracks on new ski pole*

Figure 4.8: *Visible cracks from three point bending tests*

Figure 4.9 shows delamination and cracking of the old ski pole at 5 mm from the loading point. The maximum extent of delamination and through thickness cracks for the old ski pole was 25 mm from the loading zone.

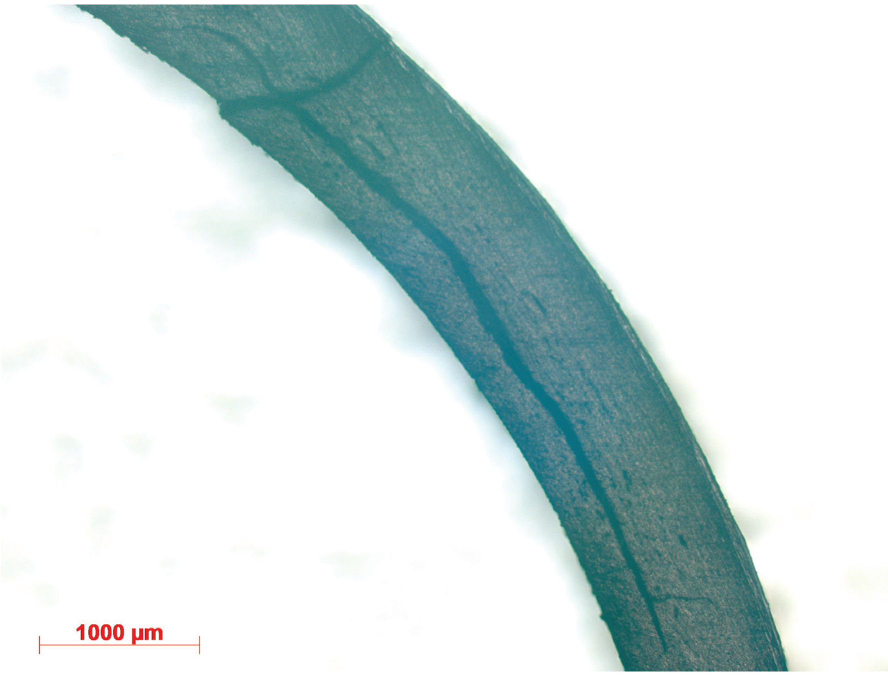

Figure 4.9: *Microscopy of failure of the old ski pole,* 5 mm *from the loading point*

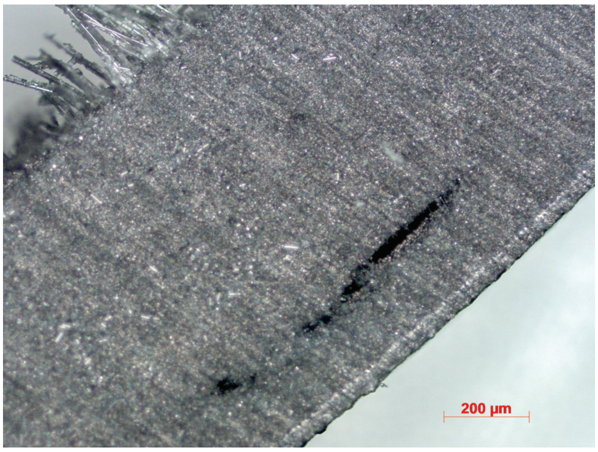

(a) *Delamination*

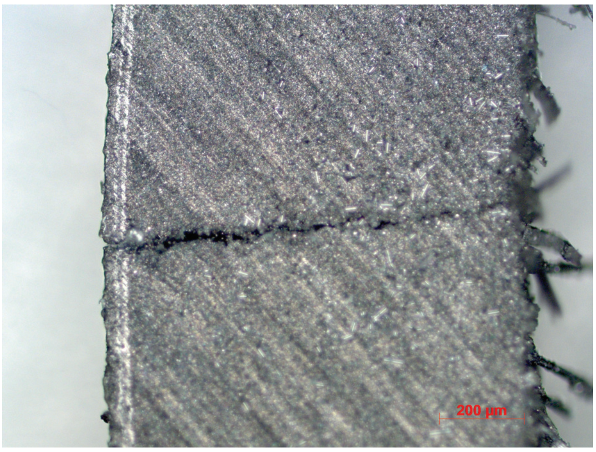

(b) *Crack through the thickness*

Figure 4.10: *Microscopy of failure of the old ski pole,* 25 mm *from the loading point*

Analyzing the failure of the new ski pole no longitudinal cracks could be found except from at the loading point where the laminate had been crushed. The microscopy analysis revealed delamination up to 15 mm, as seen in Figure 4.11.

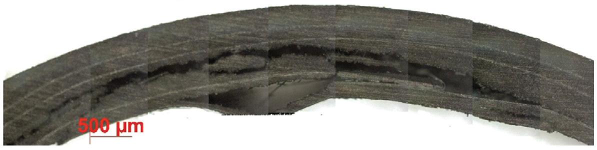

(a) *Delamination* 5 mm *from loading point*

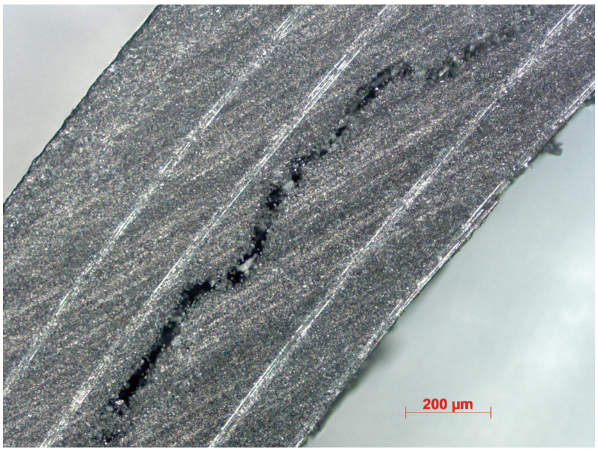

(b) *Delamination* 15 mm *from loading point*

Figure 4.11: *Microscopy images of delamination of the new ski pole*

4.6 Numerical simulations

In Figure 4.12, the maximum deflection of the pole is plotted against the axial force. In the plot, the results from the FE analysis are compared to the experimental data from Skigo.

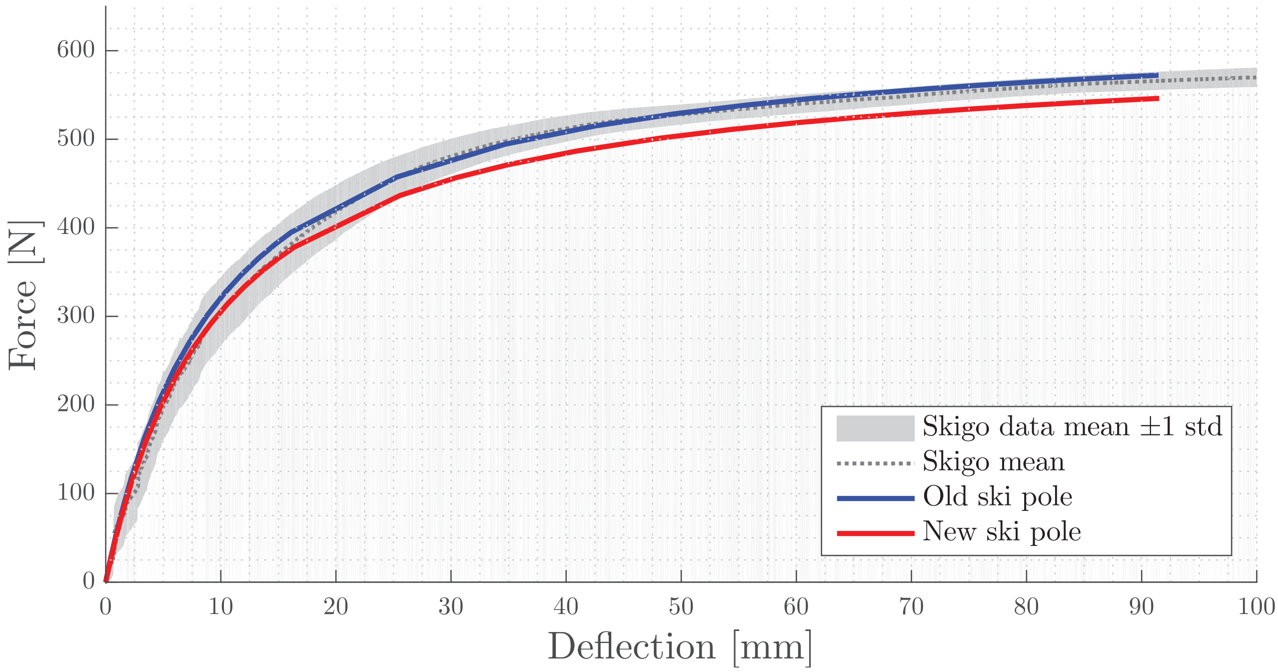

Figure 4.12: *Load-deflection curve of experimental data and FE analysis for the old and new ski pole*

In Figure 4.13, a contour plot of the deformed ski pole is seen from the Y-Z plane.

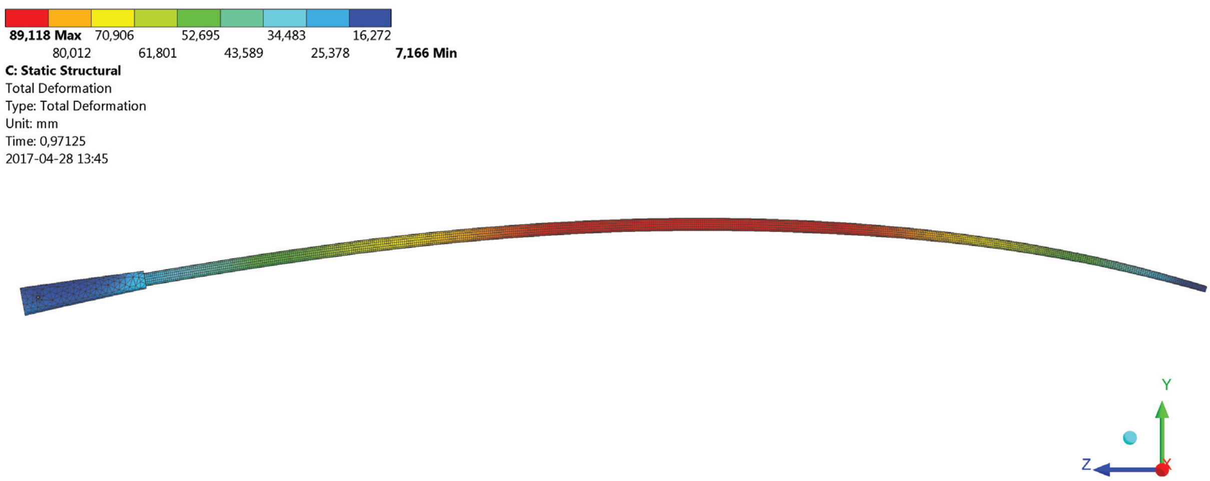

Figure 4.13: *FE contour plot of the displacements of the old ski pole*

4.6.1 Failure and damage

In Figure 4.14, 4.15 and 4.16, failure criteria for the different failure modes are presented for the old and new ski poles. The plots do not show the failure lamina-by-lamina, instead the most critical failure through the thickness is presented in the plot. Figure 4.14a and 4.14b shows fiber failure of the old and new ski pole. Both tensile and compressive failure criteria are included in the plot. Figure 4.15a and 4.15b shows matrix failure for the old and the new ski pole, again both tensile and compressive failure criteria are included. In Figure 4.16a and 4.16b the delamination criterion is shown for the old and the new ski pole respectively. Note that pink areas in the plots indicate failure.

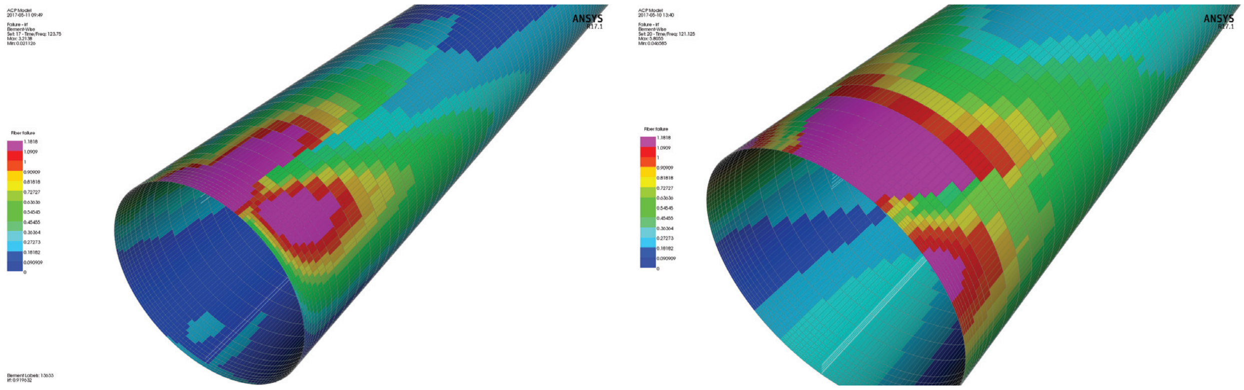

(a) *Old ski pole* (b) *New ski pole*

Figure 4.14: *Failure criteria in fiber direction. Note that pink areas indicates failure.*

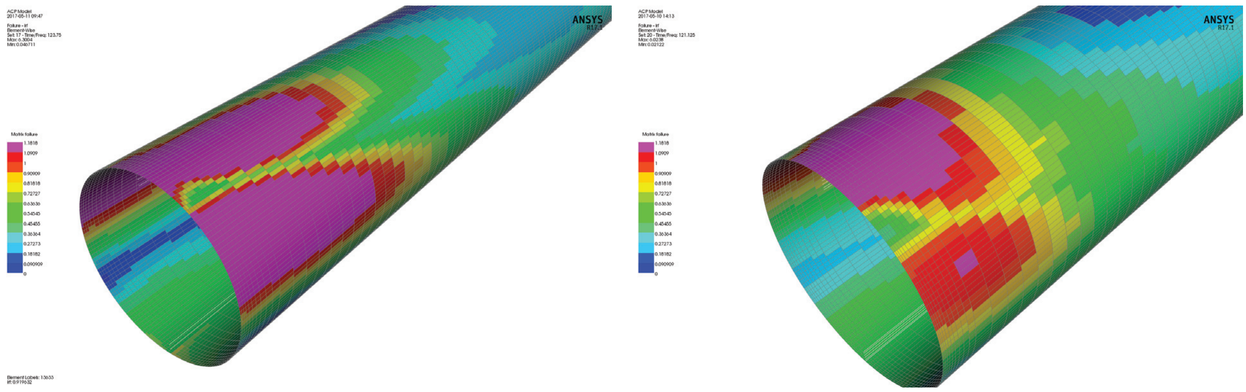

(a) *Old ski pole* (b) *New ski pole*

Figure 4.15: *Matrix failure criteria for old and new ski pole. Note that pink areas indicates failure.*

In Figures 4.18 and 4.17, the progressive damage of the old and new ski pole is presented. Due to the discrete nature of the MPDG model an element can either be damaged (red) or undamaged (blue). For the plots a degradation factor of 0.5 has been used.

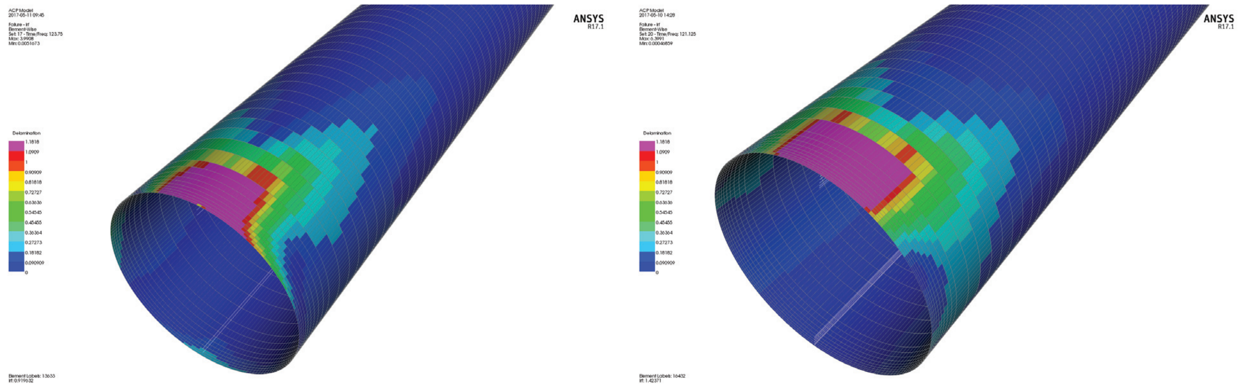

(a) *Old ski pole* (b) *New ski pole*

Figure 4.16: *Failure criterion for delamination. Note that pink areas indicates failure.*

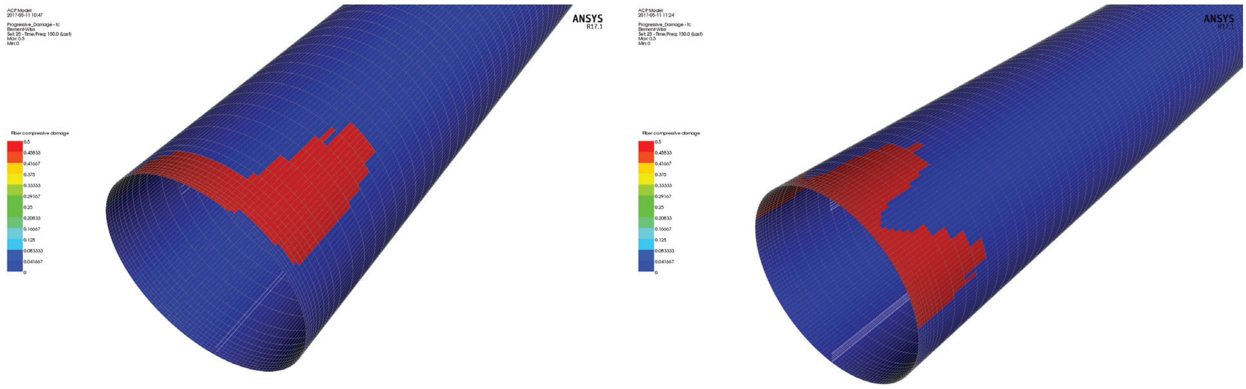

(a) *Compressive damage in fiber direction of old ski pole* (b) *Compressive damage in fiber direction of new ski pole*

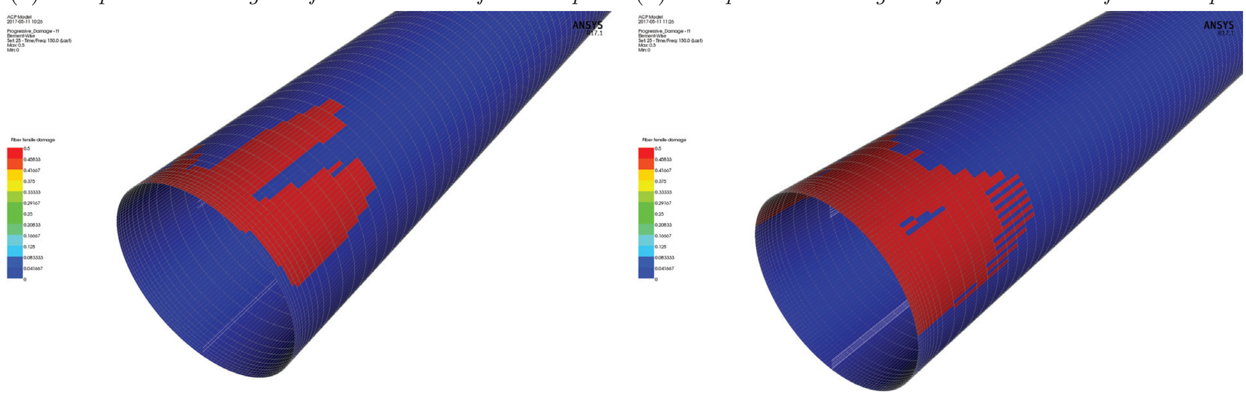

(c) *Tensile damage in fiber direction of old ski pole* (d) *Tensile damage in fiber direction of new ski pole*

Figure 4.17: *Progressive damage in the fiber direction of the old and new ski pole. Note that red areas indicates failure.*

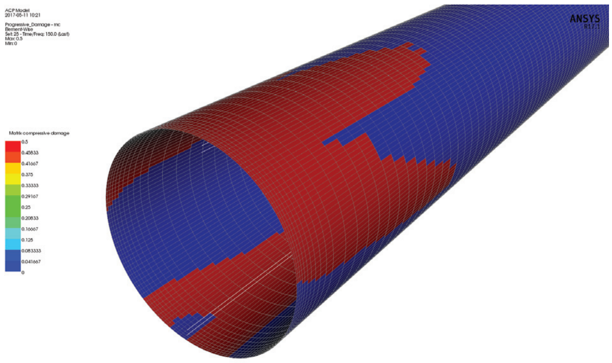

(a) *Compressive matrix damage of old ski pole*

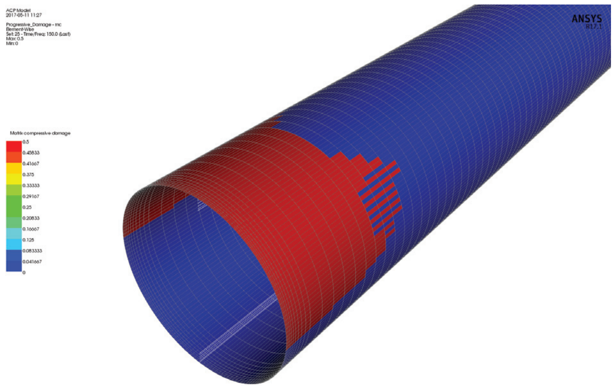

(b) *Compressive matrix damage of new ski pole*

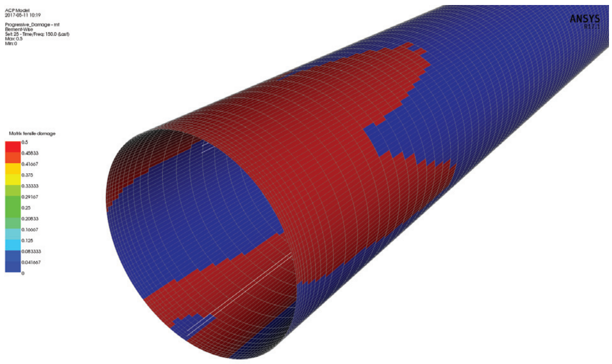

(c) *Tensile matrix damage of old ski pole*

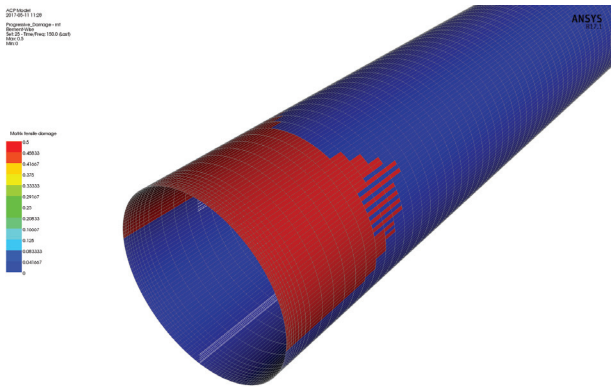

(d) *Tensile matrix damage of new ski pole*

Figure 4.18: *Progressive damage in transverse direction the old and new ski pole. Note that red areas indicates failure.*

In Figures 4.19 and 4.20 the force-displacement curves of the three point bending experiments are compared to the results from the FE analysis.

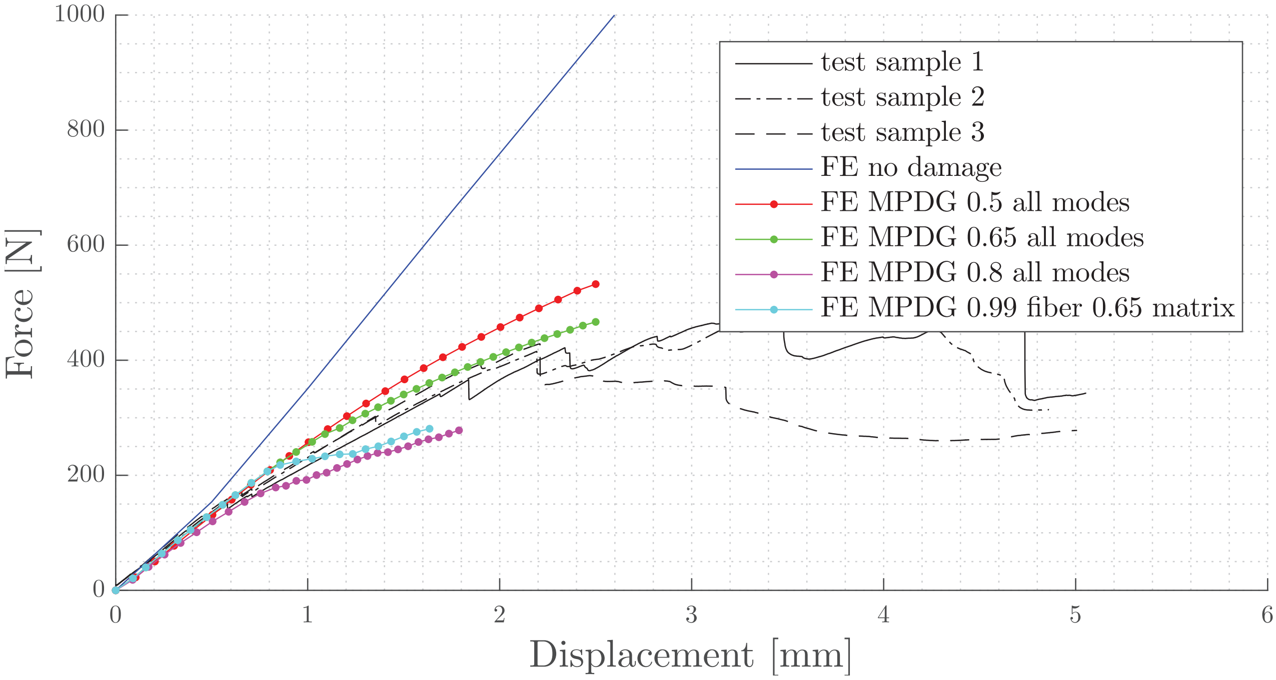

Figure 4.19: *Force-displacement curves from three point bending experiment compared to the results from the FE analysis for the old ski pole.*

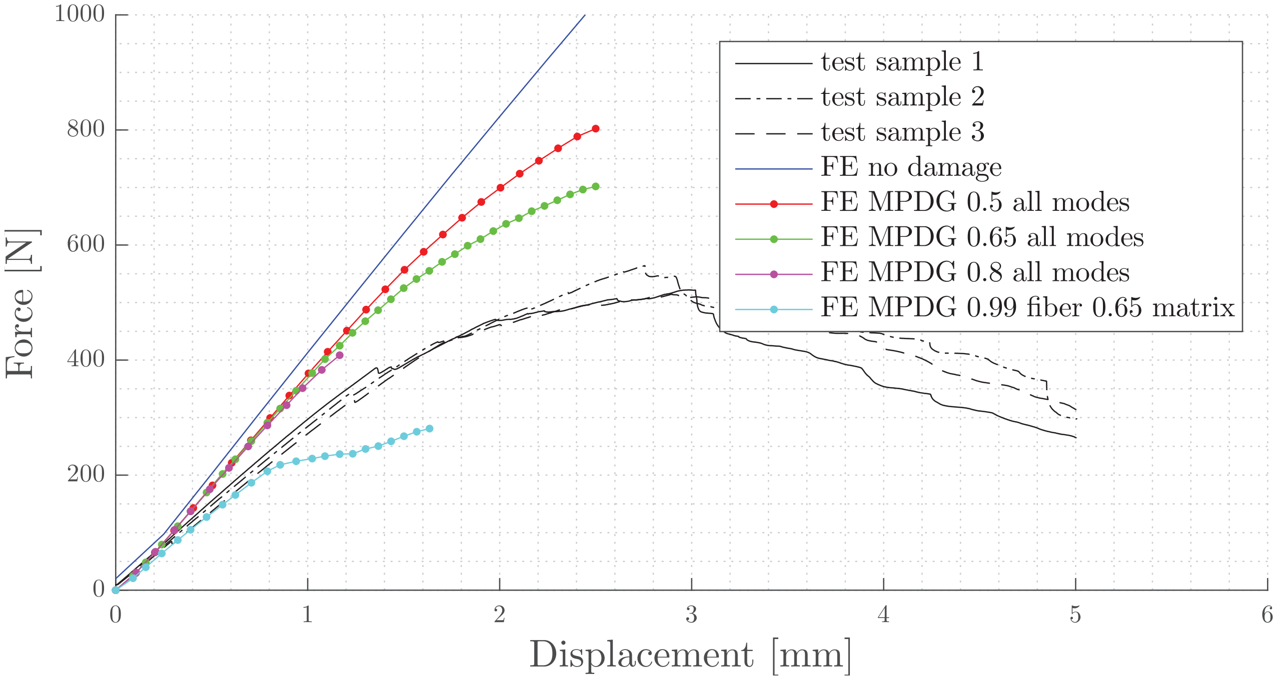

Figure 4.20: *Force-displacement curves from three point bending experiment compared to the results from the FE analysis for the new ski pole.*

5 Discussion

Part of the purpose of this thesis has been to analyze to which extent different composite lay-ups would change the performance of the ski poles. The ski poles from the different suppliers were found to have different lay-ups, making it possible to do the analysis in an experimental manner. In the following sections, a comparison of the characteristics is made.

5.1 Geometry

Analyzing the geometry gave a good understanding of how the outer diameter and the wall thickness vary along the length of the pole, see Figure 4.1 and 4.2. The measuring of the wall thickness showed that the reference ski poles has an average thickness of 1 mm, except for close to the edges where the wall thickness is thinner. The thickness varies by ±0.2 mm for the old ski pole and by ±0.1 mm for the new ski pole. These variations may seem small, but considering the average thickness of 1 mm, these variations are 20 % and 10 % of the thickness for the old and the new ski pole, respectively.

The ski poles are assumed to have been manufactured by table rolling by which pre-impregnated composite fabrics (prepreg) are rolled up on a mandrel, afterwards tape is winded around the pole to maintain pressure. It could be concluded that the old ski pole had suffered from a less precise manufacturing process. It was found that it had poor concentricity, meaning that the differences between the largest and smallest wall thickness per sampled cross section were large. This may have been a consequence of uneven pressure during the rolling, presumably since matrix material in areas subjected to a higher pressure might be pushed to low pressure areas. Local variations of the wall thickness might indicate the existence of weak spots or sections that limit the strength of the ski pole. At the final stage of production this tape is ground off, a lack of precision in this step will cause variations in thickness, as was found.

The ski poles seem to have been targeted to have the same nominal thickness. However, it seems as if the two different suppliers have produced ski poles of different quality.

5.2 Material properties testing

Overall, the experiments yielded good results, the main problem during the testing was lack of test samples and samples with desired lay-up and shape. As mentioned, only the provided ski poles were available for material testing, this limited the shape of the test specimens to a none UD tube shapes. For several testing methods a flat sample coupon with an UD lay-up is desired. Besides from preventing the tests to be performed in an optimal way, the non-UD layup required a transformation of measured properties to the local fiber oriented coordinate system. This transformation was based on the thickness of each lamina which introduced an uncertainty due to both errors in measurement of the lamina thickness as well as due to that the lamina thickness varying along the ski pole.

5.2.1 Tensile testing

The tensile tests of the ski pole samples from both the old and the new supplies yielded consistent results. The longitudinal stiffness was found to be about 146 GPa for the old ski pole and 150 GPa for the new with a coefficient of variation of 3 % and 7 % respectively, which is considered rather low. The old pole have one thin lamina with fibers in 45° direction which was estimated to make up about 7 % of the total wall thickness. The new pole had several thin 90° laminas which were estimated to make up 11 % of the wall thickness. The longitudinal stiffness of the old pole can thus be seen as the most accurate since the 45° layer has a small effect on the longitudinal stiffness. The presence of 90° layers, on the other hand had a profound effect on the longitudinal stiffness of the sample. The calculated value thus becomes very dependent on the assumption of the number of laminas in the transverse direction, see subsequent section about the lay-up. In the ski old pole the samples failed in the transverse direction due to the prohibition of Poisson's effect and in the new pole the glue failed causing pull out of the inserts.

5.2.2 Torsional testing

The shear modulus obtained from the torsional test gave more consistent results for the new ski pole than for the old ski pole. The coefficient of variation for the new pole was 8 % whereas it was 25 % for the old pole. This might be due to premature failure in the third sample of the old pole, as a cracking sound was heard early in the test procedure. Contrarily to the longitudinal stiffness, the shear modulus measured for the new ski pole should be seen as the most accurate one. This is due to the fact that the 90° laminas has the same contribution to the shear stiffness as the 0° laminas. In the same manner, the 45° lamina in the old pole has a profound effect on the shear stiffness whereas the corrected value becomes very dependent on the assumption of how many laminas in said direction there is. This can be seen in Table 4.4 where the measured global laminate shear modulus is about 45 % higher than the recalculated lamina shear modulus.

5.2.3 Compressive testing

The compression tests gave stiffness results inconsistent with the tensile tests. For the old ski pole, the stiffness was found to be 30 % lower than the stiffness obtained from the tensile test, while the stiffness for the new pole was found to be 4 % lower. A probable reason for this is the buckling effect as is illustrated in Figure 5.1. With a short specimen, this effect becomes a major contributor to the measurements from the strain gauges, resulting in a skewed stress strain relationship. The buckling effect becomes especially predominant for the old ski pole which has the majority of fibers in the longitudinal direction, providing little circumferential support. In the ASTM standard [13] used, a method for calculating the principal strains where the buckling effect is accounted for is presented. However, this method was not used since it required three strain gauges per specimen, measuring strains at 0°, 45° and 90°, resources that were not available at the time of testing.

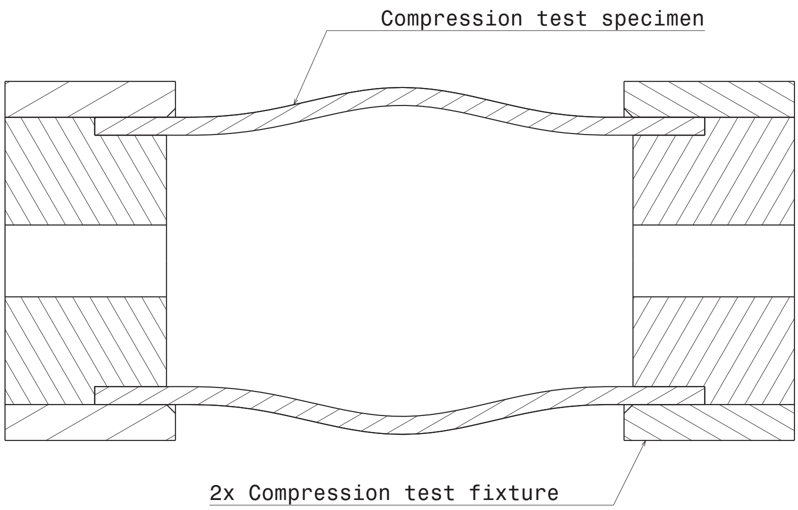

Figure 5.1: *Deformation of compression test specimen*

The ultimate stress σ'_{LU} and strain $\varepsilon'_{\mathrm{LU}}$ were calculated at the point where the test specimen were no longer able to support any load, see Figure 5.2. During the compression test, minor failures could be observed on the strain data and heard by distinct sudden clicks during the test. However, the minor failures seemed not to effect the stiffness and therefore they were neglected in the analysis.

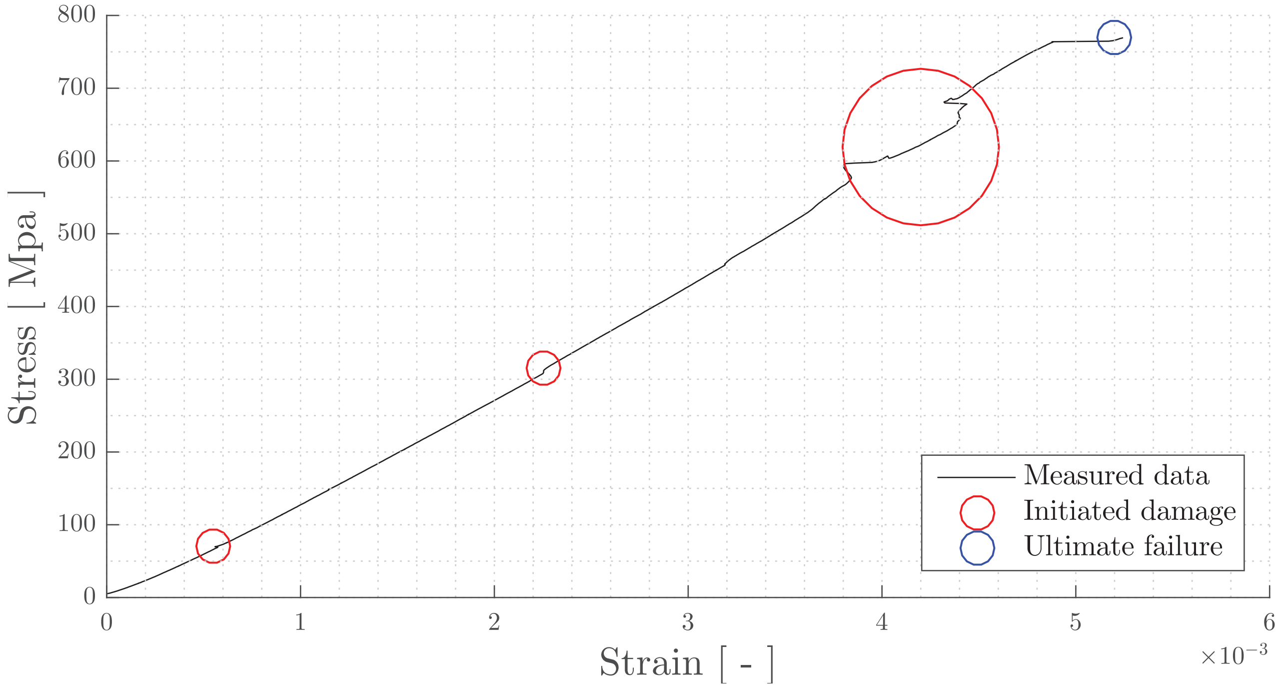

Figure 5.2: *Stress strain plot with fiber kinking*

Further, in order for the data obtained to be accurate, the failure mode had to be a pure compression failure. When testing without the fixtures the main mode of failure was crushing of the ends. This gave misleading results. In Figure 5.3 a fracture in a sample with the fixtures can be seen. As can be seen there is no crushing at the edges, instead there is a circumferential fracture as was strived for.

Figure 5.3: *Fractured compression sample with fixtures*

The ultimate compressive strains were found to be 0.57 % and 0.59 % for the old and new ski pole, respectively. These results should be considered with some care given the inaccurate measurements as described above. A conservative approach would be to account for the relative error between compression and tensile tests, whereby the maximum strain for the old ski pole would be 30 % lower, yielding a maximum strain of 0.4 %. In the same way, the maximum strain for the new ski pole would be 4 % lower meaning that maximum strain could be corrected to 0.54 %.

In the 0° laminas the ultimate stresses were found to be 607.3 MPa and 928.7 MPa for the old and the new ski pole, respectively. These were transformed from the global stress, which were calculated from the applied force and the cross-sectional area, to the local coordinate system under the assumption that the strain was constant through the thickness. However, the coefficient of variation for the old ski pole was 15.7 % indicating variations in the test data. Generally, more test specimens are needed to be in the compression tests to obtain higher statistical accuracy.

5.3 Microscopy

The microscopy analysis showed that there had been different design philosophies when designing the old and the new ski pole. For the old ski pole, the majority of fibers were found to be in 0° direction as can be seen in Figure 4.3. There was also a thin layer of 45° fibers present. For the majority of the ski pole, this layer was inside of the tube. However, at the tapered section, this layer was found on the outside. Why this thin 45° layer was included in the design remains uncertain since it does not give any obvious structural benefits.

For the new ski pole, a consistent lay-up was found through the length of the ski pole. The new ski pole seemed to be of higher quality considering the consistency of lay-up, smaller span in wall thickness spread and the lower percentage of voids in the matrix. Another finding was that the new ski pole consisted of two different types of lamina, see Figure 4.6. One lamina with large fibers of 7.1 µm in diameter and another with smaller fibers of 5.5 µm. The small fibers had a near perfect round shape whilst the large fibers had a rounded grain shape[1].

The small fibers and the fibers from the old ski pole had large similarities in shape and fiber diameter. The lamina with the large fibers had a lower volume fraction of fibers than the lamina with the small fibers. The area fraction fraction of voids was low for both laminas, about 0.02 %-0.06 %. For the old ski pole the area fraction of voids was higher at 0.73 %. It should however be noted that both poles had large coefficients of variation for the void content, which indicates that there are areas with substantially higher void content. According to [15] the void content of a good composite should be less than 1 % but can be as high as 5 % for poorly manufactured composites. A high void content creates local weaknesses, which may increase the scatter of strength properties [17], as it is seen in the experimental results. High void contents often correlates with a poor manufacturing process, as discussed in Section 5.1, which The old ski pole seems to have suffered from.

5.4 Numerical analysis

The numerical simulation proved to capture the behavior of the reference ski pole. The discrepancy between the FE analysis and the experimental data is due to several reasons. The FE analysis is based on the assumptions of laminate theory stated in Section 3.3. This implicates that the CFRP is modeled as a homogeneous orthotropic material. The experimental analysis has showed that several of these assumptions are violated, such as the laminate being free of voids, fibers being uniformly distributed and fiber and matrix being perfectly bonded. The reference ski pole also has a large variation in the wall thickness and areas with high void contents which might cause weak spots that decreases the performance of the pole.

5.4.1 Full scale bending

A crucial part of the analysis was to accurately model the loading applied from the hand strap in the full scale bending test. As described in Section 3.3.1, the compressive load is applied at an angle to the longitudinal axis. This gives rise to an additional bending moment. To model this, the load was initially applied as a remote force in this angle. However, as the load approaches the critical load, the tangential behavior of the load resulted in the load-deflection curve to approach a horizontal asymptote. This made it increasingly harder for the FE solution to converge. To overcome this problem, a simple model of the handle was incorporated to the model which gave a more accurate load transfer to the pole. The load could then be directly applied at the loading

[1] note that the diameter of the large fibers were calculated by approximating a surrounding circle whereby a small error was introduced.

point in the handle via a remote displacement of the support point making the load case more similar to that of the test rig used to generate the experimental data. Using displacement control of the handle resulted in less problems with convergence, as it does not involve finding a unique solution for a given force. Instead, the force could be obtained as the reaction force in a post-processing step.

Another problem with the loading is the placement of the support point and the loading point. The loading point is defined as the point where the force of the hand strap is transferred to the handle. This point was approximated by splitting the handle with a saw and estimating where the strap fastening mechanism locks onto the strap.

The support point is defined as the point where the hand strap is attached to the sled in the Skigo test rig. This point is of more importance as its location has a big influence on the bending moment induced by the load. The position of this point was hard to estimate as the only reference given was a video showing the test rig performing a test on a Skigo Race 2.0 ski pole. It was deduced, however, that the support point was located a bit offset from where the strap exits the handle. In order to evaluate the location of this point, a Latin hypercube design of experiments [19] was performed which incorporated 25 design points for coordinates $Y \in (-15, -22)$ mm and $Z \in (1450, 1465)$ mm in the global coordinate system. The set of coordinates matching the experimental data best was chosen, although it remains uncertain if these coordinates represent those in the experiment. However, the change of position for this point was an efficient tool for calibrating the FE model.

Comparing the results from the FE model to the experimental data given by Skigo shows that the FE model generates accurate results, both in terms of the displacement magnitude and the bending behavior of the ski pole. The new ski pole, of which there were no experimental data, was found to be less stiff than the old ski pole. This is due to the different lay-up strategies found between the ski poles. The old ski pole has more fibers in the longitudinal direction making it more resilient to bending.

5.4.2 Three point bending

The three point bending test was a tool for quantifying the impact resistance of a ski pole, with the assumption that an impact can be simplified to a quasi-static event. The actual damage from the three point bending was hard to evaluate without more advanced techniques such as x-ray or ultrasound equipment.

From the force-displacement curve, Figure 4.7, a sudden jump in the curve could be seen. Thus it was possible to estimate at which load the first failure occurred. After the first failure, the sample continued to carry the load until reaching a plateau. For the fractures to be comparable, all tests were stopped at 5 mm. The main objective with the FE damage analysis was to load to the level at which first failure occurred in the experiment to see if a similar load-deflection curve and damage severity could be seen. Ansys has two models for modeling progressive damage in composites, MPDG model mentioned in Section 3.3.2 and a Continuum Damage Mechanics (CDM) model. The advantage with the CDM model is that a damage can progress within an element and along the mesh which is more realistic than the MPDG model which assumes an element to be damaged or not based on a failure criterion only. Both models showed problems with convergence but for the MPDG model it was possible to achieve convergence by lowering the degradation factor. Several simulations were then run with an increasing degradation factor, see Table 3.3, until that the solution was no longer converging. The simulations were run up to 2.5 mm loading for which a full convergence was reached for both the old and the new ski poles for degradation factors up to 0.65. For the remaining factors, only partial convergence was reached, as can be seen in Figures 4.19 and 4.20. For the old ski pole, a degradation factor of 0.65 for all modes yielded a good match of the experimental data. A higher degradation generated a solution less stiff than what is found with the experiments. An interesting note is that the simulation with 0.99 degradation of the stiffness in the fiber direction and 0.65 degradation in the transverse direction gave virtually the same force-deflection as with 0.65 factor for all modes up to about 0.8 mm. At that point the solution for 0.99 degradation becomes much less stiff than the other, indicating onset of fiber damage at that point.

For the new ski pole, none of the simulations gave a good overall match with the experimental data. All simulations except for one generated solutions that were too stiff compared to the experimental results. The simulation with 0.99 reduction in the fiber direction and 0.65 in the transverse direction showed a good match up to about 0.8 mm where the solution becomes much less stiff than the experimental results. The big loss in the stiffness indicates heavy onset of fiber damage at that point and also indicates that the new ski pole model is more sensitive to fiber degradation factor, compared to the old ski pole. In the simulation with 99 % fiber stiffness reduction the response immediately becomes much less stiff. The reason for this is probably due to the 90° layers causing the hoop strength to not only be dependent on the transverse stiffness of the material. The same reason also makes the model more responsive to the reduction of the fiber stiffness as the fiber failure will decrease the stiffness both in the longitudinal and the transverse direction. The new pole is thus much more resistant to ovalization of the cross section which increases its performance in the three point bending compared to the old ski pole. In the old ski pole, which most fibers in the longitudinal direction, the hoop strength is basically the same as the transverse strength which gives very poor resistance to ovalization. This is seen in the simulations as the initial response appears to be governed primarily by the transverse stiffness, as the fiber degradation factor appears to have low influence. As seen in Figure 4.19, there is very little difference between the simulation with an overall stiffness reduction by 65 % and with a fiber stiffness reduction by 99 % and transverse stiffness reduction by 65 %. The difference can first be seen at about 0.8 mm load which would indicate onset of fiber damage.

The MPDG model proved to capture the stiffness of the response in the three point bending, however, it is hard to relate it to a specific physical phenomena making the model very specific for this very case. The failure mode in the experiment is a combination of several modes due to crushing, high out-of-plane stresses and delamination. For an experiment with a known failure mode, it would be possible to more accurately relate a specific factor to a certain failure mode. In the simulations, reduction factors from 0.5 to 0.99 were used. Something in between would have given the best results, which in some sense becomes un-physical, e.g. if tensile failure in the fiber direction occurs, the stiffness should theoretically go down to zero in that direction. The solution with a reduction factor of 0.65 that gave a good match is thus merely a curve fitted to experimental data as it lacks a physical ground for the damage mechanics. A more physical and reasonable model might be obtained by the CDM model that uses the actual energy release rate of the material to determine the damage progression.

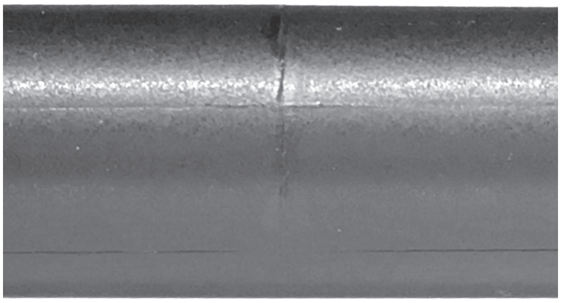

(a) *Visible cracks, including tensile matrix cracks, on the old ski pole*

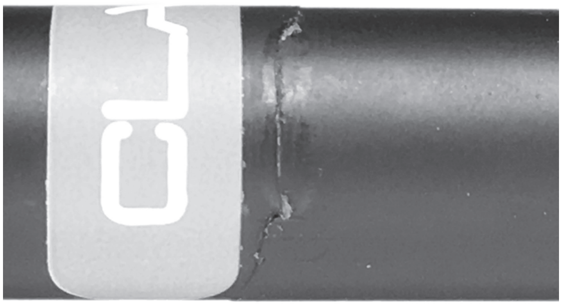

(b) *Visible cracks on the new ski pole*

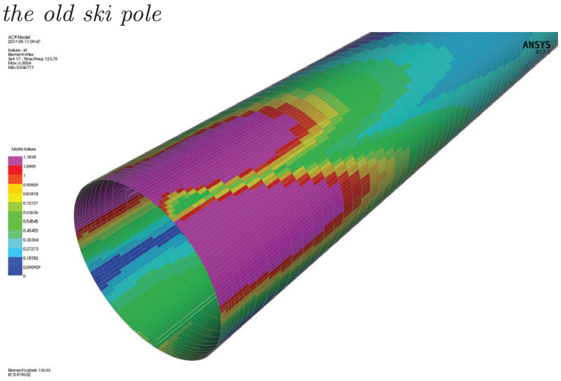

(c) *Matrix failure criteria for the old ski pole*

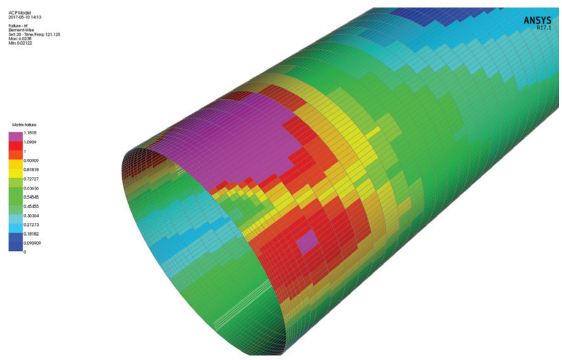

(d) *Matrix failure criteria for the new ski pole*

Figure 5.4: *Comparison of predicted matrix failure and visble cracks on test samples*

However, some correlation between the simulations and the experiments could be seen. In Figure 5.4 the predicted matrix failure is compared to the visible cracks of sample from the three point bending test. In old ski pole, longitudinal cracks runs from the loading zone on top of the pole and on each side, see Figure 5.4a. These are assumed to be matrix cracks due to transverse tensile failure, which correlates well with the simulations that indicate that tensile matrix damage along the top and the sides, as seen in Figure 5.4c. No longitudinal cracks could be seen in the new pole, Figure 5.4b, which is thought to be due to the 90° laminas which increases the hoop strength. During the loading there is considerable ovalization of the cross section which induces stresses in the circumferential direction. In the old pole which has mainly fibers along the pole the hoop strength is determined by the transverse strength, which is considerably lower than for the new ski pole where the 90° laminas greatly increases the hoop strength. This leads to the observed matrix failure in the old ski pole and to increased fiber failure in the new ski pole as the circumferential load is absorbed by the fibers instead. In both poles the transverse cracks can be seen at the loading zone which is assumed to indicate fiber failure as they run through the thickness and across the fibers, the same can be seen in the simulations as the fiber damage is concentrated at the loading zone. A assumed delamination was also seen in the old and new pole up to 25 mm and 15 mm from the loading zone. The delamination was also predicted by the Hashin delamination criteria but only up around 7 mm from the loading zone. Due to time constraints no proper delamination simulation was done which could have helped to improve the results of the FE analysis.

6 Concept design

The FE models built for the reference ski poles were used as tools to evaluate performance of new ski pole concepts. The concept pole design had a target of being more impact resistant, while maintaining weight and stiffness properties as the reference ski poles.

To understand what to design for in terms of impact resistance, two impact scenarios where identified; the damage propagation and the excessive bending load scenarios. The damage propagation scenario is when the ski pole has been handled improperly before use or a sudden impact initiates a damage which, once the ski pole is loaded, propagates until the ski pole suffers total collapse. The other scenario is when the ski pole is being excessively loaded in bending during use. This can for example be from another skier stepping on the ski pole. Knowing what to strive for in terms of design objectives, the three point bending test and the full scale bending test could be used to quantify the results for stiffness and impact resistance.

6.1 Thin-ply CFRP

Utilizing a thin-ply (<50 µm) CRFP such as TeXtreme®, from the company Oxeon, comes with many advantages in terms of stiffness, strength and weight. Using thin-ply CFRP allows for more optimized laminates since more orientations can be arranged per laminate thickness. Research has also shown that the thin-ply CFRP laminates exhibit a higher ultimate tensile strength (+10 %) than conventional thick-ply CRFP [20]. Thin-ply composites also show increased resistance to intralaminar crack propagation. According to linear elastic fracture mechanics the strength of a composite subjected to intralaminar failure is proportional to the square root of the crack size which is bounded by surrounding laminas. This is commonly called the in-situ effect [20].

The TeXtreme® is a woven reinforcement with unidirectional thin-ply CFRP stripes. The thickness of these stripes used in the weave can be alternated such that a lamina can either be balanced or unbalanced. A balanced weave has the same amount of fibers in both in-plane directions, opposed an unbalanced weave which does not. An advantage with unbalanced laminas is that they can be tailor-made for the application. With the knowledge from experiments that the longitudinal fibers are the main contributor to ski pole stiffness and that the transverse fibers improve the impact resistance, a good balance would be crucial for the new concept. Suggested by Oxeon, a TeXtreme® 76 gsm M30SC epoxy matrix lamina was a suitable material for the concept. The given data, which is to remain confidential, was for a balanced weave. Since an unbalanced weave was of interest the properties for an unbalanced product were recalculated using the rule of mixtures as

$$E_{\mathrm{z}} = \frac{1}{2}E_{\mathrm{L}} + \frac{1}{2}E_{\mathrm{T}} \Rightarrow E_{\mathrm{L}} = 2E_{\mathrm{z}} - E_{\mathrm{T}} \tag{6.1}$$

where the transverse stiffness E_T is assumed to be equal to the out of plane stiffness $E_{T'}$. Ideally, data for this particular sheet configuration would give the most accurate material properties. However, since such data did not exist, the recalculation procedure was the best possible assumption, and also the recommended method by Oxeon. The longitudinal and shear strength was taken as that of the weave whereas the transverse strength was taken from separate data for a TeXtreme® UD provided by Oxeon.

Modeling of the unbalanced lamina is done by creating a laminate where the directional properties is controlled by the lamina thicknesses. The weave was configured with 88 % longitudinal fibers and 12 % transverse fibers. This gave a weave with similar proportions of fibers as the new reference ski pole, since this ski pole was considered to have a good balance. In Ansys the weave was simplified as two layers of with perpendicular fiber directions. Thus, only the properties of the thin-ply weave was utilized and not any other effects that comes with a weave. Further, the weave was configured with 8.78 µm of 90° stripes and 64.41 µm of 0° stripes arranged as perpendicularly, yielding a total weave/lamina thickness of 73.2 µm, same thickness as the balanced laminate suggested by Oxeon.

During the three point bending experiments it was observed that the wall of the ski pole samples was crushed, see Figure 4.8. This was the main mechanism in the failure mode, not failure due to global bending. Thus it is of interest to increase the local strength of the wall. If the wall is thought of as a plate, it becomes clear that increasing the wall thickness will increase the bending stiffness of the plate and thereby the maximum load. The impact resistance was thus thought be further increased by increasing the wall thickness of the ski pole. To increase the wall thickness without adding any significant weight a sandwich structure was introduced, see Figure 6.1.

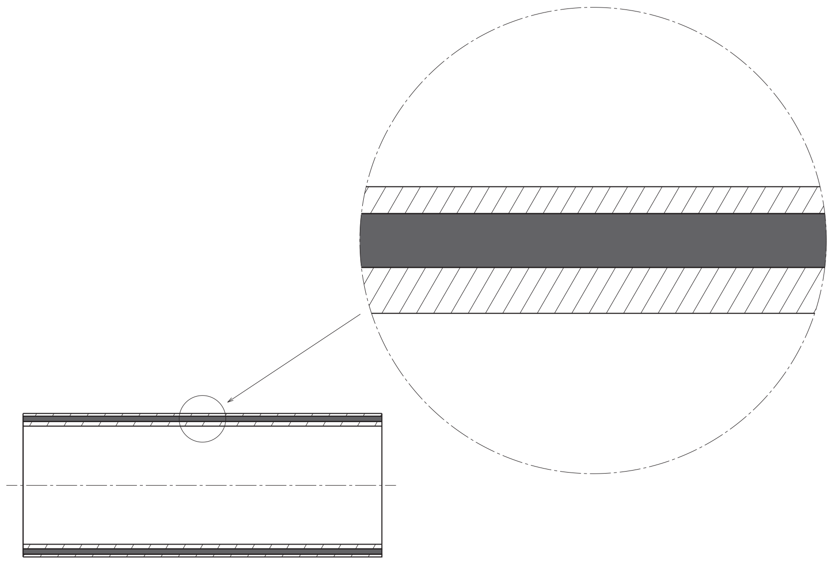

Figure 6.1: *Illustration of sandwich structure of the concept ski pole*

A foam core was added in between two laminates of TeXtreme® reinforced epoxy. The core itself consisted of a 0.6 mm ROHACELL® 71 RIMA [21] by suggestion from Oxeon. In order to accommodate the increased wall thickness and to maintain the global bending stiffness the pole diameter was increased to 17 mm

Two types of concepts for new pole design were investigated, one which is a pure laminate design and one which is a sandwich design as alluded to above. For each concept several lay-up sequences and balances were considered and evaluated for the concepts where the main objective was to maintain the weight and the bending stiffness as measured in the full scale bending test, however only the final lay-ups are presented here. The final and most promising layup of the concept was $[0F_{12}]$ with a total weight of 92.26 g whereas the final layup of the sandwich concept was $[0F_4/Core/0F_7]$. Note that the lay-ups specified with the unbalanced weave, denoted F, with the 0° direction having the majority of the fibers. The total weight of the concept ski pole is 87.7 g. The total weight penalty of using a foam core is 3 g. The target weight was the average reference ski pole weight of 88.7 g.

6.2 Concept performance

Following sections presents the simulation results for the proposed concepts. Note that the concept without the foam core is referred to as the “laminate concept” while the concept with the foam core is referred to as the “sandwich concept”.

6.2.1 Stiffness

Figure 6.2 shows that the laminate concept has similar stiffness than the reference ski poles, as was targeted. When introducing the foam core one lamina was eliminated to maintain the requirement on weight. This reduction was compensated for by increasing the diameter. The stiffness performance was similar to the performance of the concept ski pole.

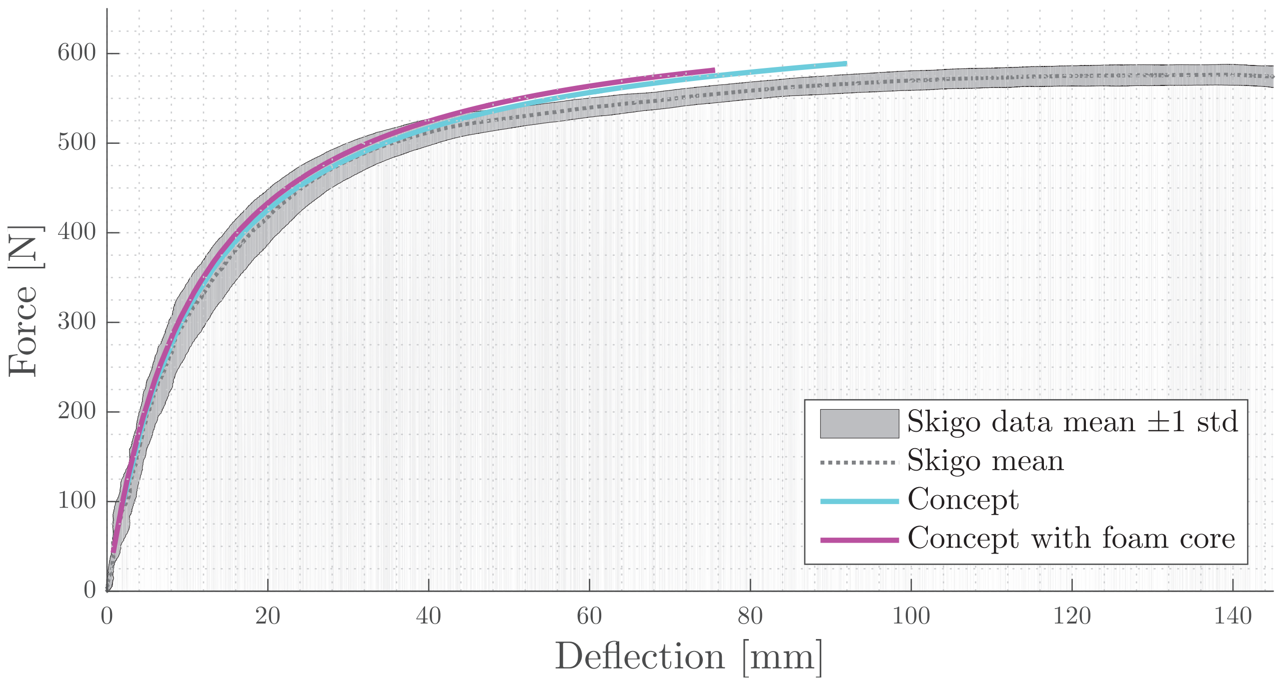

Figure 6.2: *Load-deflection curve of experimental data and FE analysis concept ski poles*

6.2.2 Impact resistance

In Figure 6.3 and Figure 6.4 the failure criteria for different failure modes are presented for the laminate concept and the sandwich concept. Included is also the new ski pole for comparison. For each failure mode the most critical value through the thickness is shown, thus less severely damaged laminas exists. The figures contains contour plots of failure criteria in the longitudinal direction and the transverse direction, the plots show both compressive and tensile failure modes.

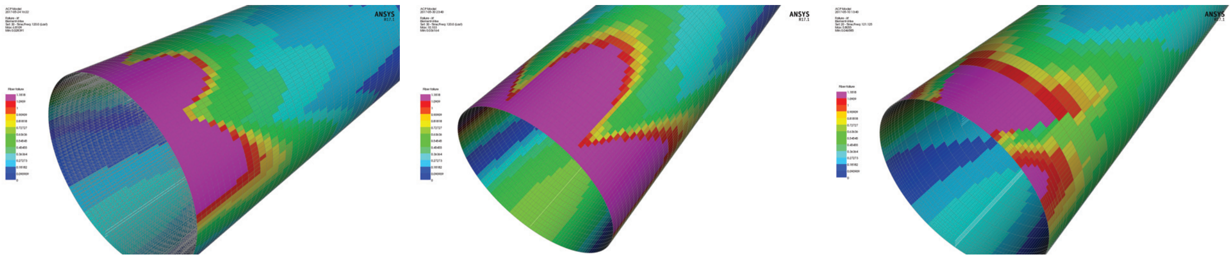

(a) *Concept ski pole with foam core* (b) *Concept ski pole* (c) *New ski pole*

Figure 6.3: *Comparison of predicted fiber failure of the concepts and the new ski pole. Note that a pink area indicates failure*

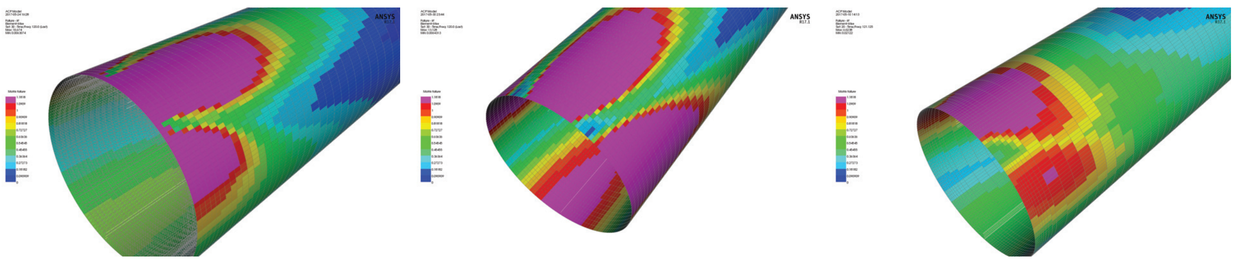

(a) *Concept ski pole with foam core* (b) *Concept ski pole* (c) *New ski pole*

Figure 6.4: *Comparison of predicted matrix failure of the concepts and the new ski pole. Note that a pink value indicates failure*

At a first glance it appears as the concept ski poles has more predicted failure than the reference ski pole. This is due to the plots showing the worst case through the thickness. If the failure is investigated lamina-by-lamina it is found that the majority of the fiber failure is predicted in the 90° laminas and the majority of the matrix failure is predicted in the 0° laminas. Looking at the 0° laminas, much less fiber failure is predicted. Most importantly, no failure is predicted in four laminas for both of the concepts, as compared to the new reference ski pole where no failure was indicated only in one lamina, see Figure 6.5. This indicates that there is more structural integrity remains in the concept ski poles, implying that they are more impact resistant.

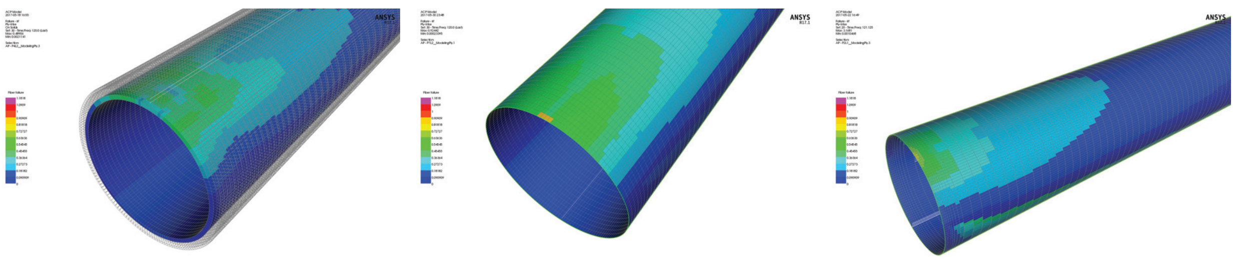

(a) *Concept ski pole with foam core* (b) *Concept ski pole* (c) *New ski pole*

Figure 6.5: *Lamina with least predicted failure of current ski pole and the concept ski pole*

For both the new reference ski pole and the concept ski poles the predicted fiber failure is mainly in the 90° laminas which further implicates the correlation between increased hoop strength and impact resistance. In the same manner, the matrix failure is mainly found in the 0° laminas due to the circumferential stresses. Failure in the circumferential direction, fiber or matrix, will have little influence on the longitudinal stiffness causing the predicted residual bending stiffness to be higher. Both of the concepts have four laminas with no indicated fiber failure, but the concept with the foam core has less predicted failure overall indicating less damage overall after an impact.

The concept with the foam core will become susceptible to core failure which would decrease the benefits gained from the increased wall thickness. From the FE simulation, the most prevalent mode of failure is for the core, as seen in Figure 6.6. The failure mode investigated in the simulation is core shear failure which is a common failure mode of sandwich structures subjected to bending [22]. During bending the laminates will mainly be subjected to compression or tension normal stresses whereas the core will experience mainly shear stresses. The failure mode implicates a loss in shear load resistance which in turn destabilizes the surrounding laminates. This will not only decrease the bending stiffness of the ski pole but will also make the laminates more susceptible to buckling. This risk, however, is mainly determined by the thickness of the laminates and the core. In the concept ski pole the core is 0.6 mm whereas the outside surrounding laminates are 0.29 mm and the inside laminate is 0.51 mm which is of comparable thickness of the core. This will decrease the risk of buckling but further analysis is required to quantify this risk. It is possible to increase the shear strength and stiffness of the core by using a higher density foam.

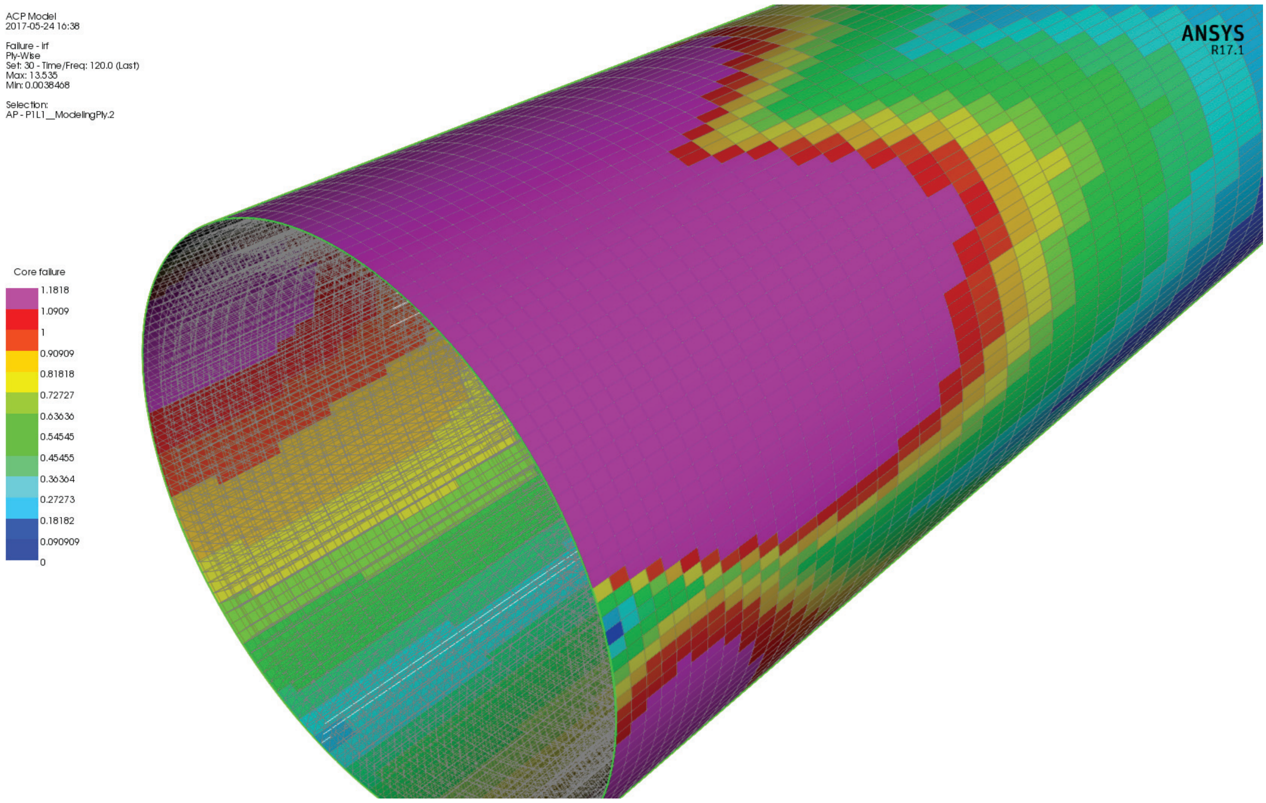

Figure 6.6: *Predicted core shear failure*

6.3 Considerations for the concept

Initial simulations proves the concepts to improve impact resistance while maintaining weight and stiffness compared to the reference ski poles. The proposed concept is innovative on many levels, to our knowledge no ski pole manufacturer has yet used thin-ply CFRP in a ski pole application. However, thin-ply CFRP has been used in similar sporting applications such as hockey blades, hockey sticks and floorball sticks. Also, the use of a foam core in the application is unheard of. It must be noted that the models for the damage initiation and progressive damage are only valid for relative comparison, since they are not physical.

Further, the concept has to be tested prototypes for verification of the simulations. Since the simplifications of the weave introduced in the model some characteristics of the TeXtreme® weave are lost. Also, with the added foam core, the new concept consists of three layers of material. This introduces further complexity to the manufacturing process that has to be accounted for.

7 Conclusions

The experiments for characterization of material properties provided good material properties data. To further increase accuracy of this data, more Tensile/Torsion and compression experiments must be conducted. Ideally these tests would be conducted in higher accordance with standards in terms of geometry. If raw material from manufacturers could have been obtained it would have been beneficial for the experimental accuracy.

The FE model of the full scale bending test proved successful in capturing the bending behavior of the ski poles within one standard deviation of experimental data. The models for damage initiation and progressive damage were matched to the three point bending test data. However, the models required input that where not physical in order to fit the data. Despite this, the models could be used for relative comparisons. For more accurate results, more advanced damage models would need to be used. Such models requires detailed material data which can only be obtained from dedicated experiments.

The FE models and experiments show that the composite lay-up is of great influence on ski pole performance. There is a trade-off between impact resistance and stiffness. Laminas in the 0° direction increase the stiffness while 90° laminas improve the impact resistance. To achieve an optimum lay-up, both orientations (and possibly others) must be combined. The newer reference ski pole proved to have a good balance of orientations.

Simulations show that the impact resistance can be increased, while maintaining weight and stiffness, by the utilization of thin-ply CFRP. Simulations also indicate that impact resistance can be further increased by the use of a foam core. However, some caution must be taken when analyzing the concept, since material data for the unbalanced weave is not verified. Also the model includes simplifications on the modeling of the weave structure. To verify the models prototypes must be manufactured and tested. When verified, more alternation of weave configurations and core materials can be evaluated.

Regardless of how the ski pole is designed with regard to material, it is crucial that that manufacturing method is able to produce poles at the right quality. Introducing high void contents or large variations in wall thickness will decrease both strength and impact resistance.

References

[1] C. Danielsson M. Johansen E. Lenning C. Olofsson. "Slagtåligare längdskidstav för elitskidåkare". 2016. URL: http://publications.lib.chalmers.se/records/fulltext/237549/237549.pdf.

[2] Martin Fagerström. *Lecture notes: Composite Mechanics*. Division of Material and Computational Mechanics, Department of Applied Mechanics, Chalmers University of Technology, 2015.

[3] *Hashin Failure Criterion*. June 5, 2017. URL: https://www.sharcnet.ca/Software/Ansys/17.0/en-us/help/acp_ug/hashin_fail_crit.html.

[4] *Core Failure*. June 5, 2017. URL: https://www.sharcnet.ca/Software/Ansys/16.2.3/en-us/help/acp_ug/Core_Failure.html.

[5] *Material Damage*. May 3, 2017. URL: https://www.sharcnet.ca/Software/Ansys/17.0/en-us/help/ans_mat/mat_damageall.html.

[6] Bengt Sundström. *Handbok och formelsamling i Hållfasthetslära*. KTH, KTH Solid Mechanics, 2010.

[7] Fredrik Larsson and Kenneth Runesson. *INTRODUCTION TO FINITE ELEMENT ANALYSIS OF PLATES*. Course literature TME245 FEM Structures, Chalmers University of Technology, 2014.

[8] Robin Olsson. Mass criterion for wave controlled impact response of composite plates. *Composites. Part A, Applied science and manufacturing* **31** (8 2000), 879–887. DOI: 10.1016/S1359-835X(00)00020-8.

[9] *Catia V5*. Feb. 1, 2017. URL: https://www.3ds.com/se/produkter-och-tjaenster/catia/produkter/catia-v5/portfoelj/.

[10] *MATLAB - MathWorks*. Feb. 1, 2017. URL: https://se.mathworks.com/products/matlab.html.

[11] *Hough transform*. Mar. 24, 2017. URL: https://se.mathworks.com/help/images/ref/hough.html.

[12] *Axson-technologies*. Feb. 7, 2017. URL: http://www.axson-technologies.com.

[13] ASTM international. *[ASTM D5449/D5449M.16] Standard Test Method for transverse compressive properties of hoop wound polymer matrix composite cylinders*. 2016.

[14] *ANSYS Composite PrePost: Composite Simulation*. Feb. 1, 2017. URL: http://www.ansys.com/products/structures/ansys-composite-preppost.

[15] Lawrence Broutman Bhagwan Agarwal and K. Chandrashekhara. *ANALYSIS AND PERFORMANCE OF FIBER COMPOSITES*. John Wiley and Sons, Inc., 2006. ISBN: 978-0-471-26891-8.

[16] Fredrik Larsson. *A short note on finite elasticity*. Course literature TME250 FEM Solids, Chalmers University of Technology, 2016.

[17] Anders Eriksson Mikeal Swerén Mikeael Therell and Hans-Christer Holmberg. Testing method for objective evaluation of cross-country ski poles (2013). DOI: 10.1007/s12283-013-0139-6.

[18] *SHELL181*. Apr. 5, 2017. URL: https://www.sharcnet.ca/Software/Ansys/16.2.3/en-us/help/ans_elem/Hlp_E_SHELL181.html.

[19] *Latin hypercube sample*. May 24, 2017. URL: https://se.mathworks.com/help/stats/lhsdesign.html.

[20] R. Amacher J. Cugnoni J. Botsis L. Sorensen W. Smith C. Dransfeld. Thin ply composites: Experimental characterization and modeling of size-effects. *Composites Science and Technology* **101** (2014). ISSN: 0266-3538. DOI: https://doi.org/10.1016/j.compscitech.2014.06.027.

[21] *Rohacell Rima*. June 21, 2017. URL: http://www.rohacell.com/sites/lists/RE/DocumentsHP/ROHACELL-RIMA-mechanical-properties-EN.pdf.

[22] D. Zenkert. *An Introduction to Sandwich Construction*. Department of Lightweight Structures, Royal Institute of Technology, 1993.

[23] *Structures: FEA Simulation ANSYS*. Feb. 1, 2017. URL: http://www.ansys.com/products/structures.

[24] *SOLSH190*. Apr. 26, 2017. URL: https://www.sharcnet.ca/Software/Ansys/16.2.3/en-us/help/ans_elem/Hlp_E_SOLSH190.html.

[25] *The Shear Properties of Unidirectional Carbon Fibre Reinforced Plastics and their Experimental Determination*. Mar. 8, 2017. URL: http://naca.central.cranfield.ac.uk/reports/arc/cp/1381.pdf.

A Sample preparation for microscopy

To obtain microscopy images the samples have to be polished, this is a tedious process, expected time is about 4 hours.

The main steps in the process are

1. Prepare the specimens
2. Cast the specimens
3. Polish the specimens

Prepare the specimens

Ensure that the surface that is to be analyzed in a microscope is flat, large deviations will take long time to flatten during the polishing process. Also make sure that the specimen is completely dry.

Cast the specimens

Casting the specimen will make the polishing easier since the casting will fit in the holders on the polishing machines and it will also hold the specimen intact. The choice of casting material is not critically important since its only purpose is to act as a fixture for the specimen. Using *CaldoFix-2* resin epoxy the following procedure can be used when casting using a vacuum chamber:

1. Mix the resin and hardener in a 25:7 ratio, mix for 5 min
2. Put the specimen in an rubber cup, place the cup in a vacuum chamber, such as *Struers CitoVac*.
3. When chamber has depressurized pour the resin using provided tubes, controlling the flow with the valve on the *CitoVac*. Let it sit for one minute.
4. Harden the casting in 80° for 60 minutes.

Polish the specimens

Using a rotating disk machine , such as the Struers *Tegrapol-31*, the polishing is done by gradually decreasing the roughness of the grinding paper. Starting at a 240 grid paper access resin can be removed until the specimen is exposed. Proceeding from this stage the roughness of the paper is decreased step wise as 320 $\rightarrow$ 400 $\rightarrow$ 600 $\rightarrow$ 800 $\rightarrow$ 1200 with 3 min increments. The step time can be shortened if the scratches from the grinding stage are even across the surface. When polishing it is important to apply some pressure on the casting, the pressure should be slightly higher closer to the center of the rotating disk for the grinding to be even.

When the last step of grinding is done one can proceed to polishing, using a Struers *Tegrapol-21* the castings can be mounted and the polishing process is automated. Polishing the carbon fiber samples using the following method yielded good results; polishing 5 min with a 9 µm polish, followed by 7 µm polish, followed by 3 µm polish for an additional 5 min. At this point the polishing is good enough for clear images in in the microscope. Though, if striving for perfection final polish with an 0.5 µm polish for 6 min can be done.

After removing the specimens from the polishing machine pouring water or methanol on the polished surface will provide a clean surface when dried.

B Matlab script for fractions analysis

```
%%%%%%%%%%%%%%%%%%%%%%%%%%%%%%%%%%%%%%%%%%%%%%%%%%%%%%%%%%%%%%%%%%%%%%%%%%%%
% Area fraction fiber, matrix and void of CFRP microscopy images
% Master Thesis: Improved ski pole design by thin ply CFRP
% Martin Granlund and Gustav Graesberg
% Chalmers University of Technology
% Department of Applied Mechanics
% Division of Material and Computational Mechanics
% Gothenburg 2017-02-27
%%%%%%%%%%%%%%%%%%%%%%%%%%%%%%%%%%%%%%%%%%%%%%%%%%%%%%%%%%%%%%%%%%%%%%%%%%%%
clear variables
close all
clc
% add path for images using addpath
% addpath('pathname')
I_org=imread('Image.filetype');

% choose which part of the image to be analyzed, use GUI
% [I_crop,rect]=imcrop(I_org);

J=rgb2gray(I_org);% convert to greyscale
% analyzed image
figure
subplot(1,3,1)
imshow(J)
title('Analyzed image')

% fiber area: turn into binary image, threshold set using graythresh
level_fiber=graythresh(J);
% level_fiber=1.4*level_fiber;

bw=im2bw(J,level_fiber);%imbinarize recommended,introduced in matlab 2016

% image of the fibers in white and matrix and voids in black

subplot(1,3,2)
imshow(bw)
title('Fibers')

fiber_area1=regionprops(bw,'area'); % gives area of each object
fiber_area2=bwarea(bw); % no. of pixels


% void area
% new binary with lower threshold to differantiate between
% matrix and void in image
level_void=0.3;
bw_void=im2bw(J,level_void);
% image of the voids

subplot(1,3,3)
imshow(bw_void);
title('Voids')

A_tot=size(J,1)*size(J,2);
void_area=A_tot-bwarea(bw_void);
% Calculate area fractions
A_org=size(I_org,1)*size(I_org,2);

matrix_area=A_tot-fiber_area2;

Af=fiber_area2/(A_tot);
Am=matrix_area/(A_tot);

Av=void_area/A_tot;
A_frac_tot=A_tot/A_org; % fraction of total image analyzed if
                        % image is cropped
```

```
area_fractions=1e2*[Af,Am,Av,A_frac_tot]';

rownames={'Fiber';'Matrix';'Void';'% of total image'};
area_table=table(area_fractions,'RowNames',rownames)
```

C Matlab script for fiber diameter analysis

```
%%%%%%%%%%%%%%%%%%%%%%%%%%%%%%%%%%%%%%%%%%%%%%%%%%%%%%%%%%%%%%%%%%%%%%%%%%%
% Calculates fiber diameters
% Master Thesis: Improved ski pole design by thin ply CFRP
% Martin Granlund and Gustav Graesberg
% Chalmers University of Technology
% Department of Applied Mechanics
% Division of Material and Computational Mechanics
% Gothenburg 2017-02-27
%%%%%%%%%%%%%%%%%%%%%%%%%%%%%%%%%%%%%%%%%%%%%%%%%%%%%%%%%%%%%%%%%%%%%%%%%%%
% Analyzes an microscopy image of fibers, identifies circular shapes. The
% identifyed fibers are marked with a circle and an average diameter is
% calculaed from a multiple fibers.
%%%%%%%%%%%%%%%%%%%%%%%%%%%%%%%%%%%%%%%%%%%%%%%%%%%%%%%%%%%%%%%%%%%%%%%%%%%

clc
close all
clear variables

%% Setup
% Reads an example image, gets its edges and displays them

addpath('path/to/image/location')
im_original = imread('name_of_image.fileformat');
px2mm = 0.053190736895079; % conversion factor pixels/mm

im_grayscale = rgb2gray(im_original);
threshold = graythresh(im_grayscale);
im_bw = im2bw(im_original,threshold);

e = edge(im_bw, 'canny');

%% Carry out the HT

radii = 70:1:100; % expected radius of fibers in pixels
h = circle_hough(e, radii, 'same', 'normalise');

%% Find some peaks in the accumulator

peaks = circle_houghpeaks(h, radii, 'nhoodxy', 15, 'nhoodr', 21, 'npeaks', 50);

%% Look at the results

imshow(im_original)
hold on;
for peak = peaks
    [x_in, y_in] = circlepoints(peak(3));
    plot(x_in+peak(1), y_in+peak(2), 'g');
end
hold off
```

D Matlab script for cross section analysis

```
%%%%%%%%%%%%%%%%%%%%%%%%%%%%%%%%%%%%%%%%%%%%%%%%%%%%%%%%%%%%%%%%%%%%%%%%%%%
% Calculates cross-sectional properties
% Master Thesis: Improved ski pole design by thin ply CFRP
% Martin Granlund and Gustav Graesberg
% Chalmers University of Technology
% Department of Applied Mechanics
% Division of Material and Computational Mechanics
% Gothenburg 2017-02-27
%%%%%%%%%%%%%%%%%%%%%%%%%%%%%%%%%%%%%%%%%%%%%%%%%%%%%%%%%%%%%%%%%%%%%%%%%%%
% Identified circular shapes whereby cross sectional properties can be
% calculated
%%%%%%%%%%%%%%%%%%%%%%%%%%%%%%%%%%%%%%%%%%%%%%%%%%%%%%%%%%%%%%%%%%%%%%%%%%%

clc
close all
clear variables

%% Setup
% Reads an example image, gets its edges and displays them

addpath('path/to/image')
im_original = imread('filename.fileformat');
px2mm = 0.0384;

im_grayscale = rgb2gray(im_original);
threshold = graythresh(im_grayscale);
im_bw = im2bw(im_original,threshold);

e = edge(im_bw, 'canny');

%% Carry out the HT

radii = 100:5:600;
h = circle_hough(e, radii, 'same', 'normalise');

%% Find some peaks in the accumulator

peaks = circle_houghpeaks(h,radii,'nhoodxy',15,'nhoodr',21,'npeaks', 2);
[value,index] =min(peaks(3,:));
peaks = peaks(:,index);
%% Look at the results

hold on;
for peak_in = peaks
    [x_in, y_in] = circlepoints(peak_in(3));
 plot(x_in+peak_in(1), y_in+peak_in(2), 'g');
end
hold off
D_in = 2*max(x_in)*px2mm;


%% Calculate outer diameter

im_fill = insertShape(im_original,'FilledCircle', [peak_in(1) peak_in(2) max(x_in)+10], 'Color', 'black', 'Opaci

threshold=graythresh(im_fill);
im_fill=im2bw(im_fill,threshold);
e = edge(im_fill, 'canny');

%% Carry out the HT

radii = max(x_in):5:600;
h = circle_hough(e, radii, 'same', 'normalise');

%% Find some peaks in the accumulator
```

```
peaks = circle_houghpeaks(h, radii, 'nhoodxy', 15, 'nhoodr', 21, 'npeaks', 1,'Smoothxy',10);

%% Look at the results

for peak_out = peaks
    [x_out, y_out] = circlepoints(peak_out(3));
%     plot(x_out+peak_out(1), y_out+peak_out(2), 'g');
end
D_out = 2*max(x_out)*px2mm;

%% Plot results

close all

imshow(im_original);
hold on;
plot(x_in+peak_in(1), y_in+peak_in(2), 'g',...
     x_out+peak_out(1), y_out+peak_out(2), 'g','LineWidth',2);

% Analysis

A_in = pi*(max(x_in)*px2mm)^2;
A_out = pi*(max(x_out)*px2mm)^2;
A_cross_section = A_out-A_in;

D_in = strcat('D_{in} = ',{' '},num2str(2*max(x_in)*px2mm),{' '},'mm')
D_out = strcat('D_{out} = ',{' '},num2str(2*max(x_out)*px2mm),{' '},'mm')
A_cross_section_str = strcat('A_{cs} = ',{' '},num2str(A_cross_section),{' '},'mm^2')
A_in_str = strcat('A_{in} = ',{' '},num2str(A_in),{' '},'mm^2')
text(peak_in(1)-30, peak_in(1),[D_in;D_out;A_cross_section_str;A_in_str])
title('Cross section data')

export = [2*max(x_in)*px2mm 2*max(x_out)*px2mm A_in A_cross_section];
```